

Article

First and Second Law Thermodynamic Analyses of Hybrid Nanofluid with Different Particle Shapes in a Microplate Heat Exchanger

Kunal Sandip Garud ¹, Seong-Guk Hwang ¹, Taek-Kyu Lim ², Namwon Kim ³ and Moo-Yeon Lee ^{1,*}

¹ Department of Mechanical Engineering, Dong-A University, 37 Nakdong-Daero 550, Saha-gu, Busan 49315, Korea; 1876936@donga.ac.kr (K.S.G.); 2070392@donga.ac.kr (S.-G.H.)

² Thermal Management R&D Center, KATECH, 303 Pungse-ro, Pungse-Myun, Cheonan 31214, Korea; tklim@katech.re.kr

³ Ingram School of Engineering, Texas State University, San Marcos, TX 78666, USA; namwonkim@txstate.edu

* Correspondence: mylee@dau.ac.kr; Tel.: +82-51-200-7642

Abstract: The improvement in the quantitative and qualitative heat transfer performances of working fluids is trending research in the present time for heat transfer applications. In the present work, the first and second law analyses of a microplate heat exchanger with single-particle and hybrid nanofluids are conducted. The microplate heat exchanger with single-particle and hybrid nanofluids is analyzed using the computational fluid dynamics approach with symmetrical heat transfer and fluid flow analyses. The single-particle Al₂O₃ nanofluid and the hybrid Al₂O₃/Cu nanofluid are investigated for different nanoparticles shapes of sphere (Sp), oblate spheroid (OS), prolate spheroid (PS), blade (BL), platelet (PL), cylinder (CY) and brick (BR). The first law characteristics of NTU, effectiveness and performance index and the second characteristics of thermal, friction and total entropy generation rates and Bejan number are compared for Al₂O₃ and Al₂O₃/Cu nanofluids with considered different-shaped nanoparticles. The OS- and PL-shaped nanoparticles show superior and worse first and second law characteristics, respectively, for Al₂O₃ and Al₂O₃/Cu nanofluids. The hybrid nanofluid presents better first and second law characteristics compared to single-particle nanofluid for all nanoparticle shapes. The Al₂O₃/Cu nanofluid with OS-shaped nanoparticles depicts maximum values of performance index and Bejan number as 4.07 and 0.913, respectively. The first and second law characteristics of the best combination of the Al₂O₃/Cu nanofluid with OS-shaped nanoparticles are investigated for various volume fractions, different temperature and mass flow rate conditions of hot and cold fluids. The first and second law characteristics are optimum at higher hot fluid temperature, lower cold fluid temperature, lower hot and cold fluid mass flow rates. In addition, the first and second law characteristics have improved with increase in volume fraction.

Keywords: Bejan number; hybrid nanofluid; microplate heat exchanger; particle shape; performance index; thermodynamic analysis



Citation: Garud, K.S.; Hwang, S.-G.; Lim, T.-K.; Kim, N.; Lee, M.-Y. First and Second Law Thermodynamic Analyses of Hybrid Nanofluid with Different Particle Shapes in a Microplate Heat Exchanger. *Symmetry* **2021**, *13*, 1466. <https://doi.org/10.3390/sym13081466>

Academic Editor: Toshio Tagawa

Received: 12 July 2021

Accepted: 4 August 2021

Published: 10 August 2021

Publisher's Note: MDPI stays neutral with regard to jurisdictional claims in published maps and institutional affiliations.



Copyright: © 2021 by the authors. Licensee MDPI, Basel, Switzerland. This article is an open access article distributed under the terms and conditions of the Creative Commons Attribution (CC BY) license (<https://creativecommons.org/licenses/by/4.0/>).

1. Introduction

The nanofluids are novel working fluids which show significant improvement in thermophysical properties due to dispersion of nanoparticles into the base fluid. The nanofluids enable the superior thermal conductivity and convective heat transfer rate compared to conventional working fluids. Therefore, the research trend on applicability of nanofluids in thermal systems is a growing body of work since the last few years. The nanoparticle shapes have considerable effect on the thermal and hydraulic performance characteristics of thermal systems incorporated with nanofluids. Numerous research studies elaborate the influence of nanoparticle shapes on hydrothermal performance of single-particle and hybrid nanofluid flow in various thermal systems. The introduction is arranged as, the first paragraph summarizes various research studies on thermophysical properties of

nanofluid with different-shaped nanoparticles, the second paragraph discusses various research studies on behavior of heat transfer characteristics of single-particle nanofluid with different-shaped nanoparticles, the third paragraph summarizes various research studies to present the effect of different-shaped nanoparticles on heat transfer characteristics of hybrid nanofluid and at the end, the key research gaps and objectives of the present study are highlighted in the last paragraph.

This paragraph presents the effect of nanoparticle shapes on the thermophysical properties of nanofluids. Kim et al. have presented improvement in the thermal conductivity by 16%, 23% and 28% for BL-, PL- and BR-shaped nanoparticles, respectively, compared to Sp-shaped nanoparticles for alumina nanofluid [1]. Xie et al. have shown enhancements of 22.9% and 18.5% in thermal conductivity of CY- and Sp-shaped silicon carbide nanoparticles, respectively [2]. Similarly, Murshed et al. have also presented the superiority in thermal conductivity of CY nanoparticles compared to Sp-shaped nanoparticles [3]. Timofeeva et al. and Maheshwary et al. have proved that the Al_2O_3 and TiO_2 nanofluids with CY-shaped nanoparticles present higher thermal conductivity and that those with Sp-shaped nanoparticles present lower viscosity [4,5]. Singh et al. have reported maximum enhancement in thermal conductivity for PL-shaped silicon carbide nanoparticles [6]. Jeong et al. have concluded that the ZnO nanofluid with rectangular-shaped nanoparticles present higher thermal conductivity and viscosity compared to that with Sp-shaped nanoparticles [7]. Zhang et al. have reported the thermal conductivities of 0.2619 W/m-K and 0.2843 W/m-K for silver nanofluid with Sp and nanowire nanoparticles, respectively [8]. Nithiyanantham et al. have presented enhancement in thermal conductivity by 16% and 12%, and in viscosity by 25% and 37% for Sp- and CY-shaped alumina nanoparticles [9].

This paragraph presents the summary of single-particle nanofluid with various nanoparticle shapes in heat transfer applications. Vanaki et al. have analyzed the heat transfer and flow characteristics of SiO_2 nanofluid flow in a wavy channel for various nanoparticle shapes and concentrations. The SiO_2 nanofluid with a PL shape presents the highest enhancement in heat transfer characteristics [10]. Mahian et al. have presented the first law analysis in terms of heat transfer coefficient and Nusselt number, and the second law analysis in terms of entropy generation for alumina nanofluid with nanoparticle shapes of BL, PL, CY and BR [11]. Akbar et al. have concluded that the PL nanoparticle shape presents maximum velocity, and the BR nanoparticle shape presents maximum enhancement in thermal conductivity for nanofluid flow in non-uniform channel [12]. Bahiraei et al. have proved that the Sp, BR, BL, CY and PL nanoparticle shapes present the descending order of entropy generation for alumina nanofluid flow in microchannel heat sink [13]. Sheikholeslami et al. have presented that the PL nanoparticle shape has the highest Nusselt number compared to Sp, CY and BR nanoparticle shapes for Fe_3O_4 nanofluid in a porous curved enclosure, as well as in a porous cavity [14,15]. Nguyen et al. have concluded that the PL-shaped nanoparticles show more than 55% enhancement in heat transfer rates compared to Sp-shaped nanoparticles for CuO nanofluid flow in a wavy channel with obstacles [16]. Hatami et al. have presented that the TiO_2 nanofluid with a PL nanoparticle shape results in superior engine cooling or heat recovery performance at the higher volume fraction [17]. Kim et al. have concluded that the acetone-based Al_2O_3 nanofluid with CY-, BR- and Sp-shaped nanoparticles present lower thermal resistance by 16%, 29% and 33%, respectively, compared with pure acetone [18]. Bahiraei et al. have investigated the thermal and hydraulic characteristics of alumina nanofluid in micro plate heat exchangers, considering nanoparticle shapes of CY, OS, BR, BL and PL [19]. Vo et al. have reported that the PL-shaped nanoparticles present the highest heat transfer rate and the best performance evaluation criteria, whereas BR-shaped nanoparticles show the lowest pressure drop [20]. Khan et al. have concluded that the nanoparticle shapes of CY, PL and BR have a significant effect on temperature distribution compared to velocity distribution for copper nanofluid flow in parallel channels [21]. Raza et al. have shown that the Sp-shaped nanoparticles have a higher heat transfer rate compared with CY- and lamina-shaped nanoparticles [22].

Giressha et al. have concluded that the BL-shaped nanoparticles have a superior heat transfer rate and Sp-shaped nanoparticles have the highest entropy generation rate compared to BR-, PL- and CY-shaped nanoparticles [23]. Elias et al. have concluded that the CY-shaped nanoparticles show better heat transfer and entropy generation characteristics for shell and tube heat exchangers with and without baffles [24,25]. The PL-shaped nanoparticles show the maximum heat transfer rate and Sp-shaped nanoparticles show the minimum pumping power as concluded by Shahsavari et al. for laminar flow and that by Alsarraf et al. for turbulent flow in a mini channel heat exchanger [26,27]. Al-Rashed et al. have reported that the PL-shaped nanoparticles show the maximum entropy generation rate and Bejan number, and Sp-shaped nanoparticles show the minimum entropy generation rate for laminar flow, and reverse results are reported by Monfared et al. for turbulent flow in a mini channel heat exchanger [28,29]. Sadripour and Chamkha have presented the heat transfer and entropy generation comparison of various shapes of metallic and non-metallic nanoparticles for different nanofluids flow in a solar collector [30]. The heat flow path, heat transfer and entropy generation of CuO nanofluid with Sp-, CY-, BR- and PL-shaped nanoparticles are simulated by Liu et al. [31].

The open literature on nanofluid in heat transfer application presents that research is trending towards the hybrid nanofluids due to their improved thermophysical properties compared to single-particle nanofluids. Therefore, there are few studies which attempted to demonstrate the improvement in heat transfer performance of hybrid nanofluids under the consideration of different nanoparticle shapes. This paragraph presents the summary of various research studies on hybrid nanofluids with various nanoparticle shapes in heat transfer applications. Ghadikolaei et al. have compared the TiO₂/Cu nanofluid with CY-, BR- and PL-shaped nanoparticles and reported that the PL-shaped nanoparticles show the highest heat transfer rate [32]. Ghadikolaei et al. have also proved that the PL-shaped nanoparticles of Fe₃O₄/Ag nanofluid show the maximum heat transfer rate due to an increase in the shape factor [33]. Dinarvand et al. have investigated the heat transfer and fluid flow characteristics of TiO₂/CuO nanofluid with Sp-, CY-, PL- and BR-shaped nanoparticles and the shown maximum Nusselt number for PL-shaped nanoparticles [34]. Bhattad and Sarkar have proved that the BR- and PL-shaped nanoparticles present the best and worst hydrothermal performances, respectively, for the hybrid nanofluid with combinations of alumina, titania and copper oxide or copper with silica nanoparticles [35]. Benkhedda et al. have reported the highest heat transfer rate for BL-shaped nanoparticles and the highest friction factor for PL-shaped nanoparticles when the TiO₂/Ag nanofluid flows through a tube [36]. Ghobadi et al. have compared the magnetohydrodynamic heat transfer of hexahedron- and lamina-shaped nanoparticles for the Al₂O₃/TiO₂ nanofluid and reported that the Nusselt number is affected mostly by lamina-shaped nanoparticles [37]. Aziz et al. have proposed an inverse relation between the shape factor of the nanoparticle and heat transfer for Cu and Fe₃O₄/Cu nanofluids [38]. Ghadikolaei et al. have reported the highest heat transfer rate and Nusselt number for TiO₂/CuO and MoS₂/Ag nanofluids with BL-shaped nanoparticles because of an increase in the shape factor at a higher temperature [39,40]. Similar results are deduced for the GO/MoS₂ nanofluid by Ghadikolaei and Gholinia [41]. Maraj et al. have investigated the shape effect of nanoparticles on magnetohydrodynamic heat transfer and flow characteristics [42]. Sahu et al. have presented the energy and exergy analyses of various hybrid nanofluids with Sp-, CY- and PL-shaped nanoparticles [43].

The comprehensive literature review reveals that there is no concrete comparative study on the first and second law analyses of single-particle and hybrid nanofluids with different particle shapes in heat transfer applications. The objective of this study is to investigate the first and second law characteristics of the microplate heat exchanger incorporated with single-particle and hybrid nanofluids with different nanoparticle shapes under various volume fractions, temperatures and mass flow rates. The computational fluid dynamics approach with symmetrical heat transfer and fluid flow concept is adopted to evaluate the first and second law characteristics of the microplate heat exchanger. The

NTU, effectiveness, performance index, thermal entropy generation rate, friction entropy generation rate, total entropy generation rate and Bejan number are compared for Al_2O_3 and $\text{Al}_2\text{O}_3/\text{Cu}$ nanofluids with Sp-, OS-, PS1-, PS2-, PS3-, PS4-, BL-, PL-, CY- and BR-shaped nanoparticles. In addition, the best combination of nanofluid with nanoparticle shape to archive an optimum heat transfer performance in the microplate heat exchanger is suggested based on the first and second law characteristics.

2. Numerical Method

2.1. Computational Geometry and Boundary Conditions

The numerical investigation based on the computational fluid dynamics (CFD) approach is conducted to evaluate the first and second law characteristics of the microplate heat exchanger with single-particle and hybrid nanofluids. The three-dimensional model of the microplate heat exchanger is depicted in Figure 1. The microplate heat exchanger comprises of two flow lines in the counter flow direction, the nanofluid as hot fluid and water as cold fluid. There are three flow passages for the nanofluid and three flow passages for water. Each flow passage is divided into 17 microchannels with a cross section of $0.25 \text{ mm} \times 0.32 \text{ mm}$ for the nanofluid and that of $0.25 \text{ mm} \times 0.42 \text{ mm}$ for water. Hence, there are total 51 microchannels with a length of 12.5 mm and wall thickness of 0.52 mm for the nanofluid and water. The microplate heat exchanger is made up of copper material. The microplate heat exchanger is symmetrical, which results in symmetrical heat transfer and fluid flow through the microchannel, hence one pair of microplates for hot and cold fluids is considered as the computational geometry to reduce the computational time. The single-particle nanofluid of Al_2O_3 and hybrid nanofluid of $\text{Al}_2\text{O}_3/\text{Cu}$ with volume fractions of 0.5%, 1.0% and 2.0% are considered as hot fluid. The nanofluids are flowing with inlet temperatures of $90 \text{ }^\circ\text{C}$, $80 \text{ }^\circ\text{C}$ and $70 \text{ }^\circ\text{C}$ and inlet mass flow rates of 10 kg/h, 20 kg/h and 30 kg/h. The cold fluid water is flowing with inlet temperatures of $10 \text{ }^\circ\text{C}$, $20 \text{ }^\circ\text{C}$ and $30 \text{ }^\circ\text{C}$ and inlet mass flow rates of 10 kg/h, 20 kg/h and 30 kg/h. The pressure outlet boundary condition is applied at the outlet of the heat exchanger. The nanofluids and water enter with uniform velocity and uniform temperature. The external surfaces of the heat exchanger are assumed to be insulated and a no-slip condition is assumed at all walls of the heat exchanger. The conjugate heat transfer is considered in the present study in that the solid domain is subjected to a conduction mechanism and fluid domains are subjected to conduction and convection mechanisms. The computational geometry of the microplate heat exchanger presents a similar pattern and symmetry boundary and forms the mirror pattern and thermal and flow characteristics. Therefore, the symmetry boundary conditions are applied on the computational geometry of the microplate heat exchanger.

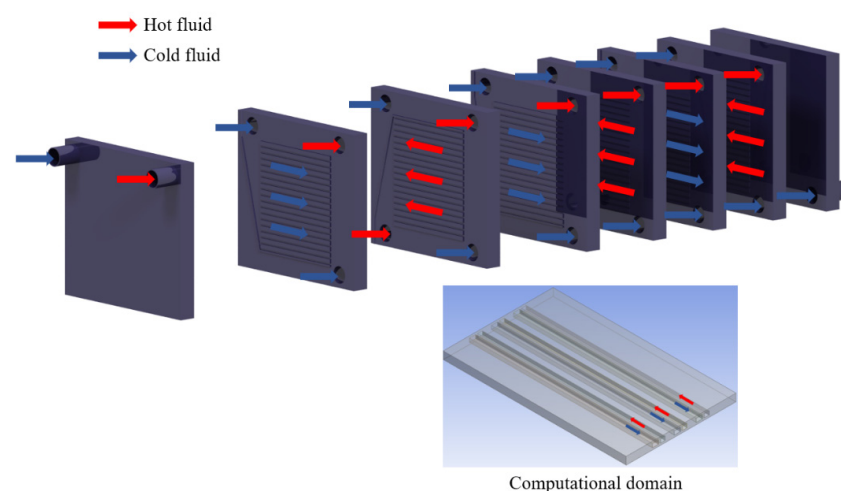


Figure 1. Three-dimensional model of the microplate heat exchanger.

2.2. Governing Equation and Meshing

The continuity, momentum and energy equations are solved using the computational fluid dynamics approach to analyze the thermodynamic attributes of the microplate heat exchanger with single-particle and hybrid nanofluids [44–46]. The continuity Equation (1) is expressed per unit of surface area (m^2). The governing equations are considered for the single pair microplates in the heat exchanger based on symmetrical heat transfer. While solving the equations, it is assumed that the flow is three-dimensional, steady, turbulent and incompressible. Additionally, the working fluids are assumed to be Newtonian [47].

Continuity equation

$$\nabla \cdot (\rho U) = 0 \quad (1)$$

Momentum equation

$$\nabla \cdot (\rho U U) = -\nabla p + \nabla \cdot (\mu \nabla U) \quad (2)$$

Energy equation for fluid domains

$$\nabla \cdot (\rho U h) = \nabla \cdot (\lambda \nabla T) \quad (3)$$

Energy equation for solid domains

$$\nabla^2 T = 0 \quad (4)$$

The working fluids in the microplate heat exchanger are exposed to heat exchange which results in entropy generation. The volumetric total entropy generation rate is the sum of the volumetric thermal entropy generation rate and the volumetric friction entropy generation rate as presented by Equation (5) [48].

$$\dot{S}_T = \dot{S}_{Th} + \dot{S}_{Fr} \quad (5)$$

The volumetric thermal entropy generation rate is calculated using Equation (6) as the summation of volumetric thermal entropy generations due to average and fluctuating temperature gradients [48].

$$\dot{S}_{Th} = \frac{\lambda}{T^2} \left[\left(\frac{\partial \bar{T}}{\partial x} \right)^2 + \left(\frac{\partial \bar{T}}{\partial y} \right)^2 + \left(\frac{\partial \bar{T}}{\partial z} \right)^2 \right] + \frac{\lambda}{T^2} \left[\overline{\left(\frac{\partial T'}{\partial x} \right)^2} + \overline{\left(\frac{\partial T'}{\partial y} \right)^2} + \overline{\left(\frac{\partial T'}{\partial z} \right)^2} \right] \quad (6)$$

The first term at the right side of Equation (6) presents the volumetric thermal entropy generation rate due to time-mean temperature gradients. Whereas, the second term at right side of Equation (6) presents the volumetric thermal entropy generation rate due to fluctuating temperature gradients, which could also be expressed as Equation (7) [48].

$$\dot{S}_{Th} = \frac{\lambda_t}{T^2} \left[\left(\frac{\partial \bar{T}}{\partial x} \right)^2 + \left(\frac{\partial \bar{T}}{\partial y} \right)^2 + \left(\frac{\partial \bar{T}}{\partial z} \right)^2 \right] \quad (7)$$

Therefore, the volumetric thermal entropy generation rate could be reduced to Equation (8) after manipulating $\lambda_{eff} = \lambda + \lambda_t$.

$$\dot{S}_{Th} = \frac{\lambda_{eff}}{T^2} \left[\left(\frac{\partial \bar{T}}{\partial x} \right)^2 + \left(\frac{\partial \bar{T}}{\partial y} \right)^2 + \left(\frac{\partial \bar{T}}{\partial z} \right)^2 \right] \quad (8)$$

The volumetric friction entropy generation rate is evaluated using Equation (9) as the summation of direct dissipation due to the average velocity gradient and indirect dissipation due to the fluctuating velocity gradient [48].

$$\begin{aligned} \dot{S}_{Fr} = \frac{\mu}{T} \{ & 2[(\frac{\partial \bar{v}}{\partial x})^2 + (\frac{\partial \bar{v}}{\partial y})^2 + (\frac{\partial \bar{v}}{\partial z})^2] + (\frac{\partial \bar{v}_x}{\partial y} + \frac{\partial \bar{v}_y}{\partial x})^2 + (\frac{\partial \bar{v}_x}{\partial z} + \frac{\partial \bar{v}_z}{\partial x})^2 + (\frac{\partial \bar{v}_y}{\partial z} + \frac{\partial \bar{v}_z}{\partial y})^2 \} \\ & + \frac{\mu}{T} 2[(\frac{\partial v'_x}{\partial x})^2 + (\frac{\partial v'_y}{\partial y})^2 + (\frac{\partial v'_z}{\partial z})^2] + (\frac{\partial v'_x}{\partial y} + \frac{\partial v'_y}{\partial x})^2 \\ & + (\frac{\partial v'_x}{\partial z} + \frac{\partial v'_z}{\partial x})^2 + (\frac{\partial v'_y}{\partial z} + \frac{\partial v'_z}{\partial y})^2 \end{aligned} \quad (9)$$

The first term on right side of Equation (9) indicates the direct entropy generation due to dissipation in the mean flow field, which is commonly denoted as direct dissipation. Whereas, the second term on the right side of Equation (9) indicates turbulent or indirect dissipation due to fluctuating velocity gradients, which is also expressed as Equation (10) [48].

$$\dot{S}_{Fr'} = \frac{\rho \beta^* k \omega}{T} \quad (10)$$

Therefore, the volumetric friction entropy generation rate could be reduced to Equation (11) [48].

$$\dot{S}_{Fr} = \frac{\mu}{T} \{ 2[(\frac{\partial \bar{v}}{\partial x})^2 + (\frac{\partial \bar{v}}{\partial y})^2 + (\frac{\partial \bar{v}}{\partial z})^2] + (\frac{\partial \bar{v}_x}{\partial y} + \frac{\partial \bar{v}_y}{\partial x})^2 + (\frac{\partial \bar{v}_x}{\partial z} + \frac{\partial \bar{v}_z}{\partial x})^2 + (\frac{\partial \bar{v}_y}{\partial z} + \frac{\partial \bar{v}_z}{\partial y})^2 \} + \frac{\rho \beta^* k \omega}{T} \quad (11)$$

Here, β^* is the model constant with value of 0.09.

The Bejan number is evaluated to quantify the contribution of the volumetric thermal entropy generation rate in the volumetric total entropy generation rate. The Bejan number (Be) is defined as the ratio of the volumetric thermal entropy generation rate to the volumetric total entropy generation rate, as presented by Equation (12) [48].

$$Be = \frac{\dot{S}_{Th}}{\dot{S}_T} \quad (12)$$

The governing equations are solved using the finite volume method and second order approach. The tetrahedron mesh elements are considered for the computational geometry of the heat exchanger and fluid domains. The inflation layers are provided on the fluid domains to consider the effect of boundary layers at the walls of the heat exchanger. The mesh independency test is carried out by generating five different mesh element numbers on the computational geometry. The results of performance index are evaluated for different mesh element numbers by considering the flow of water as hot and cold fluids. The inlet temperature and mass flow rate on the hot side are 90 °C and 20 kg/h, and those on the cold side are 20 °C and 20 kg/h. The mesh independency results for five different mesh elements are presented in Table 1. The temperature and pressure drop results for hot and cold fluids are significantly varying when the mesh element numbers are ranging from 157,649 to 732,993. However, beyond the mesh element number of 732,993, the simulated results of outlet temperatures and pressure drops of hot and cold fluids vary within $\pm 1\%$ [49]. Therefore, the computational geometry with a mesh element number of 732,993 is considered for the further numerical investigations. The mesh configuration of computational geometry with selected final mesh elements is depicted in Figure 2. The SIMPLE scheme with velocity-pressure coupling and the convergence criteria of 10^{-8} are considered for solving the governing equations.

Table 1. Mesh independency test results.

Mesh Elements	Hot Fluid-Temperature (°C)	Cold Fluid-Temperature (°C)	Hot Fluid-Pressure Drop(bar)	Cold Fluid-Pressure Drop (bar)
157,649	88.669	29.841	2.413	1.321
489,478	86.295	26.877	2.637	1.444
732,993	85.180	24.888	2.738	1.502
1,142,485	85.182	24.086	2.742	1.505
1,588,899	85.181	23.865	2.751	1.507

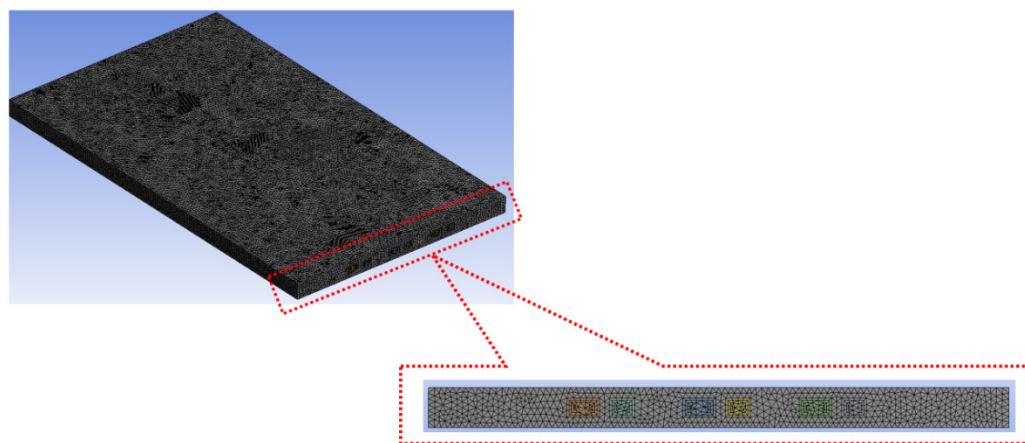


Figure 2. Mesh configuration for computational geometry.

3. Thermophysical Properties of Nanofluids with Nanoparticle Shapes

The thermophysical properties of single-particle and hybrid nanofluids with different nanoparticle shapes are evaluated using the models presented in Sections 3.1 and 3.2, respectively. The different nanoparticle shapes considered are Sp, OS, PS1, PS2, PS3, PS4, BL, PL, CY and BR, as depicted in Figure 3.

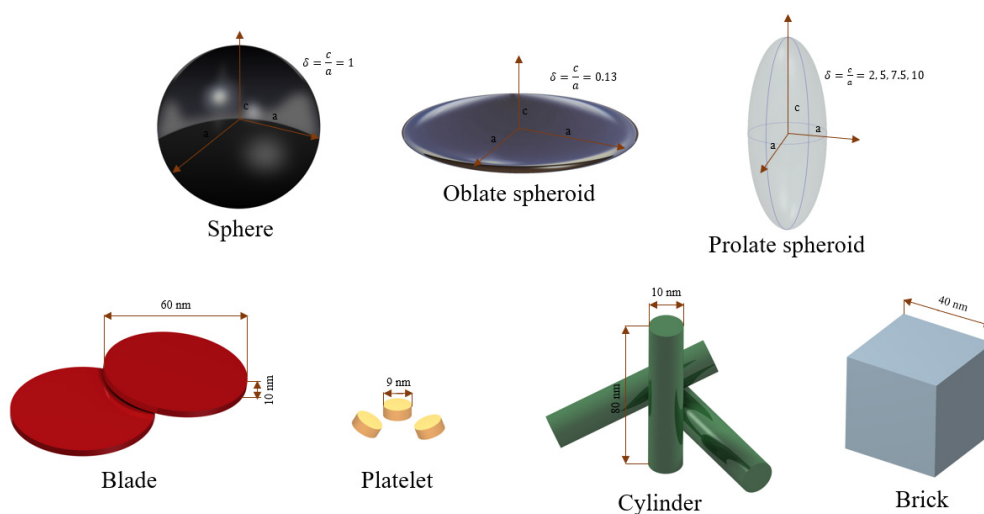


Figure 3. Different nanoparticle shapes considered in the present study.

3.1. Single-Particle Nanofluid Properties

The volume fraction of nanoparticles in nanofluid is calculated using Equation (13) [50].

$$\varnothing = \frac{V_{np}}{V_{bf} + V_{np}} \tag{13}$$

The density and specific heat of single-particle nanofluids are not affected by nanoparticle shapes and are calculated using Equations (14) and (15), respectively [51,52].

$$\rho_{nf} = (1 - \varnothing)\rho_{bf} + \varnothing\rho_{np} \tag{14}$$

$$C_{p,nf} = \frac{(1 - \varnothing)\rho_{bf}C_{p,bf} + \varnothing\rho_{np}C_{p,np}}{\rho_{nf}} \tag{15}$$

The nanoparticle shape affects the thermal conductivity and viscosity of single-particle nanofluids. The thermal conductivity of single-particle nanofluids with Sp-, OS-, PS1-, PS2-,

PS3- and PS4-shaped nanoparticles are calculated using the model proposed by Hamilton–Crosser, as presented by Equation (16). The model proposed by Timofeeva et al. [4], as presented by Equation (17), is used to calculate the thermal conductivity of single-particle nanofluids with BL-, PL-, CY-, and BR-shaped nanoparticles [53].

$$\frac{k_{nf}}{k_{bf}} = \frac{k_{np} + (n - 1)k_{bf} - (n - 1)(k_{bf} - k_{np})\varnothing}{k_{np} + (n - 1)k_{bf} + \varnothing(k_{bf} - k_{np})} \tag{16}$$

$$\frac{k_{nf}}{k_{bf}} = 1 + (C_k^{shape} + C_k^{surface})\varnothing = 1 + C_k\varnothing \tag{17}$$

Here, n is shape factor = $\frac{3}{\Psi}$. The values n for OS, PS1, PS2, PS3 and PS4 are calculated using the sphericity parameter Ψ , whose values for given nanoparticle shapes are reflected in Table 2. C_k^{shape} is the nanoparticle shape contribution to thermal conductivity, $C_k^{surface}$ is surface resistance that affects the thermal conductivity of nanofluid and influences by the solid/liquid interface.

Table 2. Parameters for calculating thermal conductivity and viscosity of spherical, oblate spheroid and prolate spheroid nanoparticle shape-based nanofluids.

Particle Shape	δ	Ψ	\varnothing_m
Sphere	1	1	0.599
Oblate spheroid	0.13	0.4904	0.575
Prolate spheroid 1	2	0.9287	0.546
Prolate spheroid 2	5	0.7321	0.432
Prolate spheroid 3	7.5	0.6453	0.368
Prolate spheroid 4	10	0.5883	0.321

The viscosity of single-particle nanofluids with Sp-, OS-, PS1-, PS2-, PS3- and PS4-shaped nanoparticles is evaluated using Equation (18). This equation is proposed by Muller et al., based on the mathematical model presented by Maron and Pierce. For calculating the viscosity of single-particle nanofluids with BL-, PL-, CY-, and BR-shaped nanoparticles, Timofeeva et al.’s [4] model, as presented by Equation (19), is used [53].

$$\frac{\mu_{nf}}{\mu_{bf}} = \left(1 - \frac{\varnothing}{\varnothing_m}\right)^{-2} \tag{18}$$

$$\mu_{nf} = \mu_{bf} \left(1 + A_1\varnothing + A_2\varnothing^2\right) \tag{19}$$

Here, \varnothing is the volume fraction of nanoparticles in nanofluid and \varnothing_m is the packing fraction, which is calculated using Equation (20) [53]. A_1, A_2 are coefficients proposed by Timofeeva et al., and values of these coefficients are extracted from references [4,53].

$$\varnothing_m = \frac{2}{(0.321\delta + 3.02)} \tag{20}$$

The aspect ratio of spheroids is expressed as Equation (21). The parameters a and c are denoted as lengths of spheroid semi-axes, which could be seen in Figure 3. For OS- and PS-shaped nanoparticles, these parameters are presented by Equations (22) and (23), respectively [53].

$$\delta = \frac{c}{a} \tag{21}$$

$$OS = 1 - \left(\frac{c}{a}\right)^2, c < a \tag{22}$$

$$PS = 1 - \left(\frac{a}{c}\right)^2, c > a \tag{23}$$

3.2. Hybrid Nanofluid Properties

The open literature lacks presentation of the concrete models for evaluating the thermophysical properties of hybrid nanofluids with different nanoparticle shapes. In the present study, the updated equations for calculating the thermophysical properties of hybrid nanofluids with different nanoparticle shapes are proposed based on equations presented in Section 3.1 and references [54,55]. The density, specific heat, thermal conductivity and viscosity of hybrid nanofluids with different nanoparticle shapes are evaluated using Equations (24)–(30).

Volume fraction of hybrid nanofluid

$$\phi_{hnf} = \phi_{np1} + \phi_{np2} \tag{24}$$

Density of hybrid nanofluid

$$\rho_{hnf} = \phi_{np1}\rho_{np1} + \phi_{np2}\rho_{np2} + (1 - \phi_{hnf})\rho_{bf} \tag{25}$$

Specific heat of hybrid nanofluid

$$C_{p,hnf} = \frac{\phi_{np1}\rho_{np1}C_{p,np1} + \phi_{np2}\rho_{np2}C_{p,np2} + (1 - \phi_{hnf})\rho_{bf}C_{p,bf}}{\rho_{hnf}} \tag{26}$$

Thermal conductivity of hybrid nanofluid

For Sp-, OS-, PS1-, PS2-, PS3- and PS4-shaped nanoparticles

$$\frac{k_{hnf}}{k_{bf}} = \frac{\frac{\phi_{np1}k_{np1} + \phi_{np2}k_{np2}}{\phi_{hnf}} + (n - 1)k_{bf} + (n - 1)(\phi_{np1}k_{np1} + \phi_{np2}k_{np2}) - (n - 1)\phi_{hnf}k_{bf}}{\frac{\phi_{np1}k_{np1} + \phi_{np2}k_{np2}}{\phi_{hnf}} + (n - 1)k_{bf} - (n - 1)(\phi_{np1}k_{np1} + \phi_{np2}k_{np2}) + \phi_{hnf}k_{bf}} \tag{27}$$

For BL-, PL-, CY-, and BR-shaped nanoparticles

$$\frac{k_{hnf}}{k_{bf}} = 1 + (C_k^{shape} + C_k^{surface})\phi_{hnf} = 1 + C_k\phi_{hnf} \tag{28}$$

Viscosity of hybrid nanofluid

For Sp-, OS-, PS1-, PS2-, PS3- and PS4-shaped nanoparticles

$$\frac{\mu_{nf}}{\mu_{bf}} = (1 - \frac{\phi_{hnf}}{\phi_m})^{-2} \tag{29}$$

For BL-, PL-, CY-, and BR-shaped nanoparticles

$$\mu_{nf} = \mu_{bf} (1 + A_1\phi_{hnf} + A_2\phi_{hnf}^2) \tag{30}$$

The parameters for calculating thermal conductivity and viscosity of nanofluids with Sp-, OS- and PS-shaped nanoparticles are shown in Table 2 [53]. The parameters for calculating thermal conductivity and viscosity of nanofluids with BL-, PL-, CY- and BR-shaped nanoparticles are shown in Tables 3 and 4, respectively [53].

Table 5 depicts the properties of the considered nanoparticles of Boehmite alumina (Al₂O₃) and copper (Cu) and the base fluid of water [19,50]. These properties are computed in equations of Sections 3.1 and 3.2 to evaluate the density, specific heat, thermal conductivity and viscosity for Al₂O₃ and Al₂O₃/Cu nanofluids with different nanoparticle shapes.

Table 3. Parameters for calculating thermal conductivity of blade, platelet, cylinder and brick nanoparticle shape-based nanofluids.

Particle Shape	Aspect Ratio	C_k	C_k^{shape}	$C_k^{surface}$
Blade	1:6:1/12	2.74	8.26	−5.52
Platelet	1:1/8	2.61	5.72	−3.11
Cylinder	1:8	3.95	4.82	−0.87
Brick	1:1:1	3.37	3.72	−0.35

Table 4. Parameters for calculating viscosity of blade, platelet, cylinder and brick nanoparticle shape-based nanofluids.

Particle Shape	Coefficients	
	A_1	A_2
Blade	14.6	123.3
Platelet	37.1	612.6
Cylinder	13.5	904.4
Brick	1.90	471.4

Table 5. Properties of base fluid and nanoparticles.

Property	Water	Alumina	Copper
Density (kg/m ³)	997.1	3050	8933
Specific heat (J/kg·K)	4179	618.3	385
Thermal conductivity (W/m·K)	0.613	30	400
Viscosity (Pa·s)	0.001003	-	-

4. Data Reduction

The amount of heat released from the hot fluid (Nanofluid) and amount of heat gained by the cold fluid (Water) are calculated using Equations (31) and (32), respectively [56,57].

The heat absorbed by the working fluid is calculated using Equation (18) [36].

$$\dot{Q}_{hf} = \dot{m}_{hf} c_{p,hf} (T_{hf,i} - T_{hf,o}) \quad (31)$$

$$\dot{Q}_{cf} = \dot{m}_{cf} c_{p,cf} (T_{cf,o} - T_{cf,i}) \quad (32)$$

The average heat exchange between hot and cold fluids is calculated using Equation (33) [58].

$$\dot{Q} = \frac{\dot{Q}_{hf} + \dot{Q}_{cf}}{2} \quad (33)$$

The overall heat transfer coefficient for the microplate heat exchanger is evaluated using Equation (34) [58].

$$U = \frac{\dot{Q}}{A \Delta T_{LMTD}} \quad (34)$$

The hot and cold fluid flows are considered as a counter flow, hence the log mean temperature difference is calculated using Equation (35).

$$\Delta T_{LMTD} = \frac{\Delta T_2 - \Delta T_1}{\ln\left(\frac{\Delta T_2}{\Delta T_1}\right)} \quad (35)$$

$$\Delta T_1 = T_{hf,i} - T_{cf,o} \quad (36)$$

$$\Delta T_2 = T_{hf,o} - T_{cf,i} \quad (37)$$

The effectiveness of the microplate heat exchanger is evaluated using Equation (38) as the ratio of actual (average) heat transfer to maximum heat transfer between hot and cold fluids [59].

$$\varepsilon = \frac{\dot{Q}}{Q_{max}} \quad (38)$$

$$\dot{Q}_{max} = C_{min} (T_{hf,i} - T_{cf,i}) \quad (39)$$

$$C_{min} = \min(C_{hf}, C_{cf}) \quad (40)$$

$$C_{hf} = \dot{m}_{hf} c_{p,hf} \quad (41)$$

$$C_{cf} = \dot{m}_{cf} c_{p,cf} \quad (42)$$

The number of transfer units (NTU) of the microplate heat exchanger is calculated using Equation (43) [59,60].

$$NTU = \frac{UA}{C_{min}} \quad (43)$$

The performance index of the microplate heat exchanger is evaluated using Equation (44) as the ratio of average heat transferred between hot and cold fluids to total pumping power [61].

$$\eta = \frac{\dot{Q}}{P_{pump}} \quad (44)$$

The total pumping power is calculated by adding the pumping powers of hot and cold fluids, as expressed in Equation (45). The pump efficiency is assumed at 80%.

$$P_{pump} = \frac{\dot{m}_{hf} \Delta P_{hf}}{0.80 \rho_{hf}} + \frac{\dot{m}_{cf} \Delta P_{cf}}{0.80 \rho_{cf}} \quad (45)$$

The total entropy generation rate (W/K) for the microplate heat exchanger is defined as the sum of the entropy generation rate due to heat transfer (W/K) and the entropy generation rate due to pressure drop (W/K). The total entropy generation rate, entropy generation rate due to heat transfer and entropy generation rate due to pressure drop are calculated using Equations (46)–(48), respectively [62,63].

$$\dot{S}_{gen,total} = \dot{S}_{gen,heat\ transfer} + \dot{S}_{gen,presure\ drop} \quad (46)$$

Entropy generation rate due to heat transfer

$$\dot{S}_{gen,heat\ transfer} = \dot{m}_{hf} C_{p,hf} \ln\left(\frac{T_{hf,o}}{T_{hf,i}}\right) + \dot{m}_{cf} C_{p,cf} \ln\left(\frac{T_{cf,o}}{T_{cf,i}}\right) \quad (47)$$

Entropy generation rate due to pressure drop

$$\dot{S}_{gen,f} = \frac{\dot{m}_{hf} \Delta P_{hf}}{\rho_{hf} T_{avg,hf}} + \frac{\dot{m}_{cf} \Delta P_{cf}}{\rho_{cf} T_{avg,cf}} \quad (48)$$

5. Results and Discussion

5.1. Validation

The experimental conditions applied by Alm et al. [64] for the same geometry and structure of the microplate heat exchanger are reflected in the present work to validate the accuracy of the numerical model. The experimental and numerical results are compared for the hot fluid inlet temperature and mass flow rate of 90 °C and 21 kg/h, respectively. The cold fluid mass flow rate ranges from 20 kg/h to 120 kg/h and the cold fluid inlet temperature is fixed at 12.5 °C for the comparison. The warm water as the hot fluid and

cold water as the cold fluid are considered for the comparison. The outlet temperatures and pressure drops of hot and cold fluids are compared for the experimental and numerical methods, as presented in Figure 4. The trends for the experimental and numerical results are same for outlet temperatures and pressure drops of hot and cold fluids. The cold fluid outlet temperature decreases with increase in the cold fluid inlet mass flow rate, which results in an increase in the hot fluid outlet temperature. Whereas, the pressure drops for hot and cold fluids have increased with an increase in the cold fluid inlet mass flow rate. Over the variation range of the cold fluid inlet mass flow rate, the maximum deviation between the experimental and numerical results of the hot fluid outlet temperature is 4.64%, that of cold fluid outlet temperature is 4.93%, that of hot fluid pressure drop is 5.64% and that of the cold fluid pressure drop is 6.49%. The numerical results are in closer agreement with the corresponding experimental results, with a maximum deviation within $\pm 10\%$ for both thermal and flow characteristics of the microplate heat exchanger. Therefore, the numerical model is valid and reliable for the detailed thermodynamic investigations on the microplate heat exchanger.

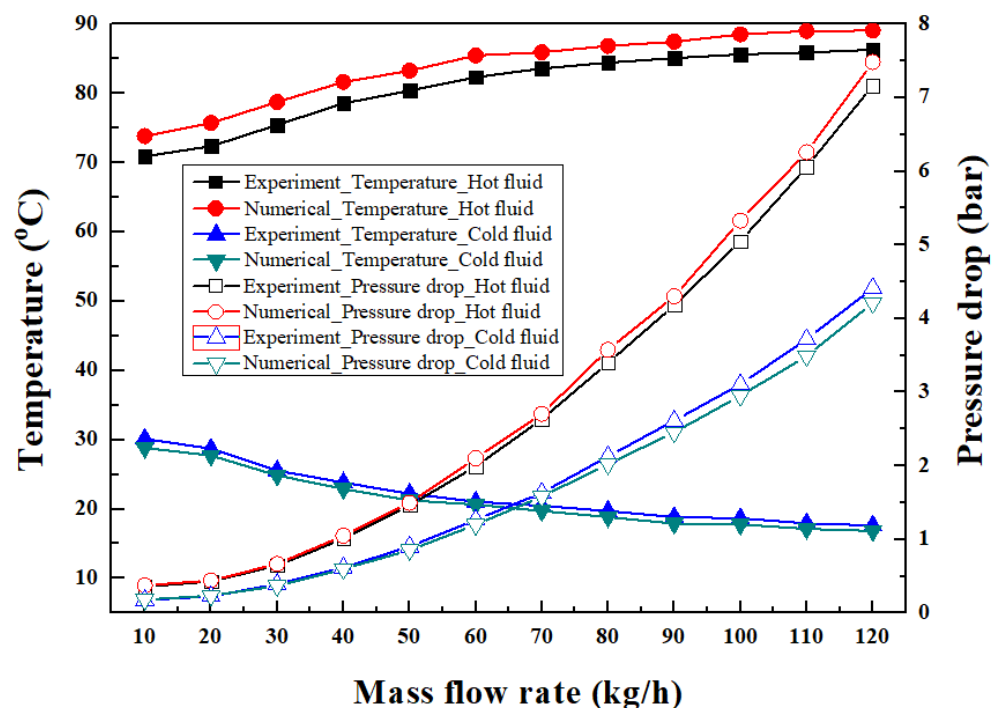
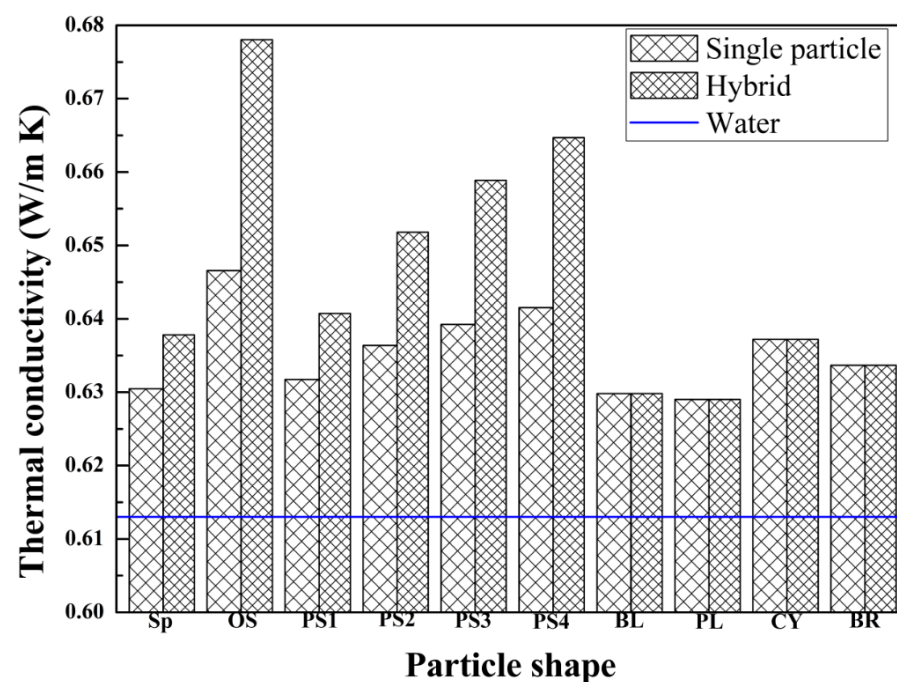


Figure 4. Comparison experimental and numerical results of temperature and pressure drop for hot and cold fluids.

5.2. Evaluation of Nanofluid Thermophysical Properties for Different Nanoparticle Shapes

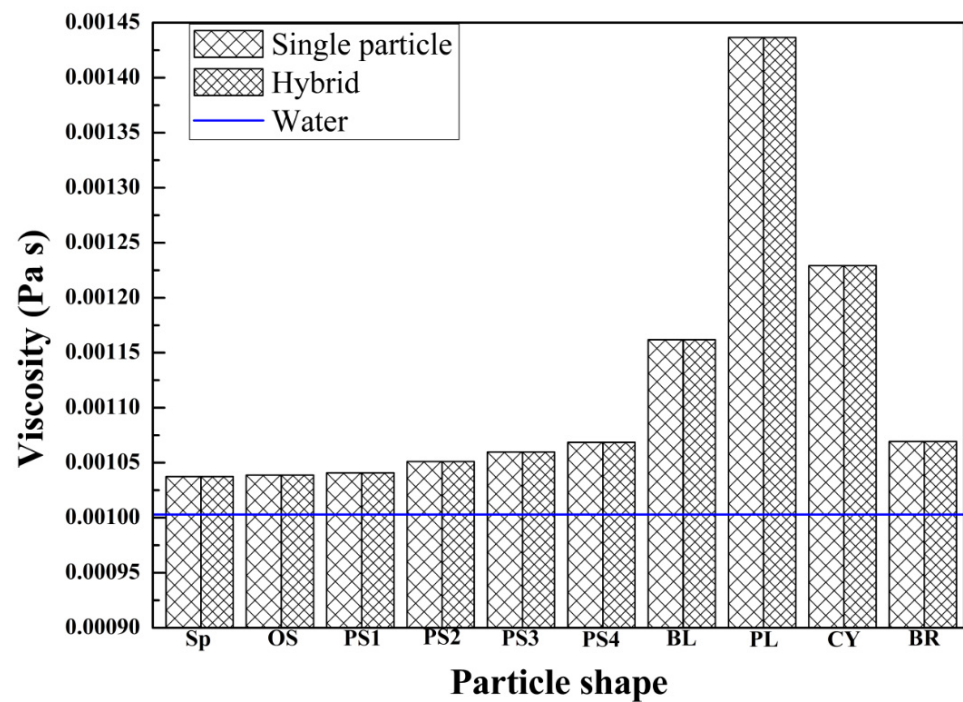
The density and specific heat are not affected by changes in nanoparticle shape, unlike thermal conductivity and viscosity. Timofeeva et al. [4] have proved that the whole area of a solid-liquid interface greatly affects the thermal conductivity and viscosity of nanofluids. Therefore, the behavior of thermal conductivity and viscosity of single-particle and hybrid nanofluids with different nanoparticle shapes are depicted in Figure 5a,b, respectively. The behavior comparison is presented for 1.0% volume fraction of the nanoparticle in both single-particle and hybrid nanofluids. The nanoparticles of Al_2O_3 and Cu are mixed in the proposition of 50–50% in the hybrid nanofluid. The stability and agglomeration of different-shaped nanoparticles significantly affect the thermal conductivity of nanofluids. The thermal conductivity of both single-particle and hybrid nanofluids with all nanoparticle shapes are superior compared to water because of dispersion of high thermal conductivity nanoparticles into the base fluid. For nanoparticle shapes of Sp, OS, PS1, PS2, PS3 and PS3, the thermal conductivity of the hybrid nanofluid are better than the single-particle

nanofluid. Whereas, in cases of nanoparticle shapes of BL, PL, CY and BR, the thermal conductivity values are the same for single-particle and hybrid nanofluids. Among all nanoparticle shapes, OS presents highest, and PL presents lowest thermal conductivity values in the respective cases of single-particle and hybrid nanofluids. The order of thermal conductivity is obtained based on the enhancement in the aspect ratio due to the fact that a rise in the contact area causes significant heat transfer when nanoparticles collide with each other [65]. Kim et al. have stated that BR-shaped nanoparticles present better thermal conductivity compared to BL-shaped nanoparticles due to rapid agglomeration [1]. The thermal conductivity values of Al_2O_3 and $\text{Al}_2\text{O}_3/\text{Cu}$ nanofluids with OS-shaped nanoparticles are higher by 5.48% and 10.61%, respectively, compared to water. The thermal conductivity of Al_2O_3 and $\text{Al}_2\text{O}_3/\text{Cu}$ nanofluids with PL-shaped nanoparticles is higher by 2.61% compared to water. The viscosity of single-particle and hybrid nanofluids with different nanoparticle shapes are higher than water because of the dispersion of nanoparticles into the base fluid. However, the viscosity values are same for single-particle and hybrid nanofluids with the same nanoparticle shape. The Al_2O_3 and $\text{Al}_2\text{O}_3/\text{Cu}$ nanofluids with PL-shaped nanoparticles present the highest viscosity among all nanoparticle shapes, which is 43.23% superior to the viscosity of water. The Al_2O_3 and $\text{Al}_2\text{O}_3/\text{Cu}$ nanofluids with Sp- and OS-shaped nanoparticles show the lowest and the second lowest values of viscosity, which are higher by 3.42% and 3.57%, respectively, compared to water. The PL-, CY- and BL-shaped nanoparticles present larger viscosity values compared to other-shaped nanoparticles due to limitation of rotational and Brownian motions. In addition, the PL- and CY-shaped nanoparticles stay in contact with one another for longer periods and interact between themselves significantly compared to other-shaped nanoparticles, which results in a higher viscosity in PL- and CY-shaped nanoparticles. Mahian et al. have presented the highest viscosity for PL-shaped nanoparticles, which increases with volume fraction [11]. The density and specific heat of the Al_2O_3 nanofluid are 1017.63 kg/m^3 and $4072.28 \text{ J/kg}\cdot\text{K}$, respectively, and those of the $\text{Al}_2\text{O}_3/\text{Cu}$ nanofluid are 1047.04 kg/m^3 and $3965.29 \text{ J/kg}\cdot\text{K}$, respectively, for all nanoparticle shapes. From this comparison, it could be concluded that the single-particle and hybrid nanofluids with OS-shaped nanoparticles have excellent thermophysical properties compared to other nanoparticle shapes.



(a)

Figure 5. Cont.



(b)

Figure 5. Behavior of (a) thermal conductivity and (b) viscosity of single-particle and hybrid nanofluids with different nanoparticle shapes.

5.3. Evaluation of First Law Characteristics for Different Nanoparticle Shapes

The comparison of NTU for single-particle and hybrid nanofluids with different nanoparticle shapes is shown in Figure 6. The NTU of single-particle and hybrid nanofluids are improved for nanoparticle shapes of Sp, OS, PS1, PS2, PS3, PS4, BL and BR compared to water because of improvement in the thermophysical properties of single-particle and hybrid nanofluids. In the case of PL-shaped nanoparticles, the NTU values are lower for both single-particle and hybrid nanofluids compared to water, due to a higher velocity of PL-shaped nanoparticles. The OS- and PL-shaped nanoparticles present the lowest and highest velocities, respectively, which results correspondingly into the lower and higher values of heat transfer coefficients. The lower velocity of OS-shaped nanoparticles results in a lower heat capacity, which dominates the lower heat transfer coefficients. Hence, as per Equation (43), it results in the highest NTU value. The higher velocity of PL-shaped nanoparticles results in a higher heat capacity and higher heat transfer coefficient; therefore, based on Equation (43), the combined effect of a higher heat transfer coefficient and a higher heat capacity presents a lower NTU for PL-shaped nanoparticles. The higher heat capacity dominates the higher heat transfer coefficient for PL-shaped nanoparticles. In the case of CY-shaped nanoparticles, the hybrid nanofluid shows superior NTU values and single-particle nanofluid shows poorer NTU values than water. In addition, for the same nanoparticle shape, the NTU of the $\text{Al}_2\text{O}_3/\text{Cu}$ nanofluid is superior to the NTU of the Al_2O_3 nanofluid due to the addition of high thermal conductivity Cu nanoparticles to the Al_2O_3 nanofluid, which results in the thermal conductivity improvement of the $\text{Al}_2\text{O}_3/\text{Cu}$ nanofluid. Bahiraei et al. have shown similar results of OS- and PL-shaped nanoparticles with the highest and lowest NTU, respectively, for single-particle nanofluids [19]. The NTU values of the Al_2O_3 and $\text{Al}_2\text{O}_3/\text{Cu}$ nanofluids with OS-shaped nanoparticles are higher by 2.86% and 6.38%, respectively, compared to the NTU of water. The Al_2O_3 and $\text{Al}_2\text{O}_3/\text{Cu}$ nanofluids with PL-shaped nanoparticles present the NTU values as lower by 3.99% and 1.82%, respectively, compared to the NTU of water.

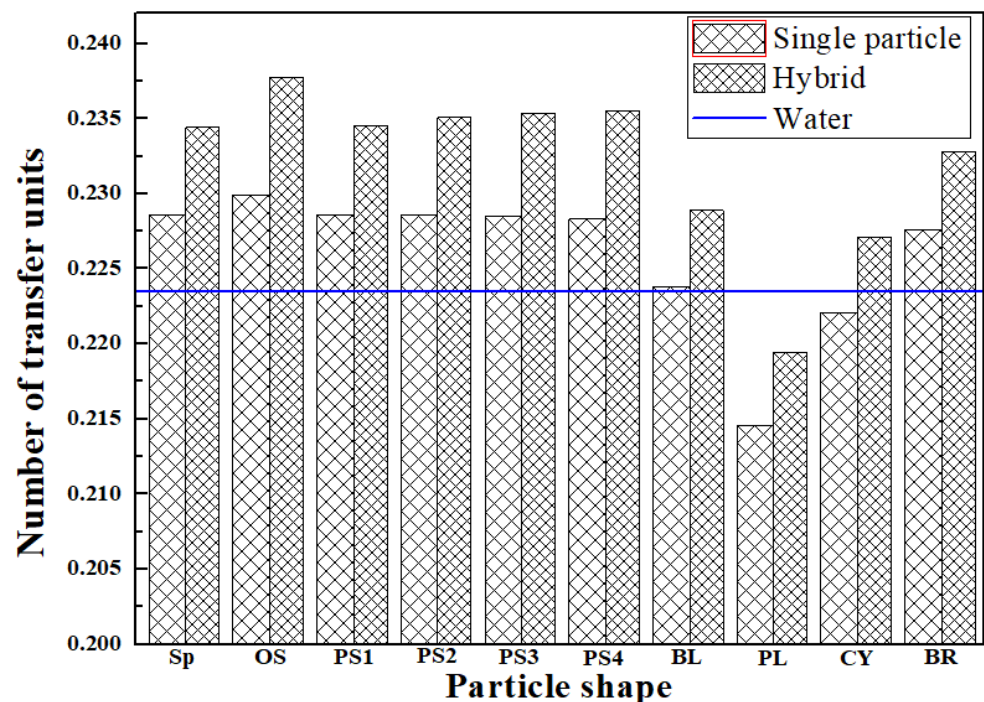


Figure 6. Comparison of NTU for single-particle and hybrid nanofluids with different nanoparticle shapes.

The effectiveness of single-particle and hybrid nanofluids with different nanoparticle shapes are compared in Figure 7. For the same nanoparticle shapes, the effectiveness of the $\text{Al}_2\text{O}_3/\text{Cu}$ nanofluid are better than the Al_2O_3 nanofluid because of an increase in the thermal conductivity of the hybrid nanofluid by the dispersion of high thermal conductivity nanoparticles. The behavior of effectiveness is same as of the NTU for single-particle and hybrid nanofluids with all nanoparticle shapes. For the single-particle nanofluids, OS-shaped nanoparticles present the highest effectiveness, followed by Sp, PS1 = PS2, PS3, PS4, BR, BL, CY and PL in decreasing order of effectiveness, in which the effectiveness of CY- and PL-shaped nanoparticles are lower than water. In the case of the hybrid nanofluid, the decreasing order of effectiveness is OS, PS4, PS3, PS2, PS1, Sp, BR, BL, CY and PL, respectively, in which the effectiveness value of PL-shaped nanoparticles is lower than water. Shahsavar et al. have also presented a lower effectiveness for alumina nanofluids with PL-shaped nanoparticles [26]. The velocity of different-shaped nanoparticles is in the inverse relation with the temperature gradient. Therefore, the lower velocity of OS-shaped nanoparticles raises the temperature variation of nanofluids, which results in higher effectiveness. The effectiveness values of Al_2O_3 and $\text{Al}_2\text{O}_3/\text{Cu}$ nanofluids with OS-shaped nanoparticles are higher by 2.75% and 6.10%, respectively, and those with PL-shaped nanoparticles are lower by 3.65% and 1.54%, respectively, compared to the effectiveness of water.

The performance index presents the combined effect of heat transfer and pressure drop characteristics. The comparison of the performance index of single-particle and hybrid nanofluids with different particle shapes is presented in Figure 8. The particle shape with the superior combination of thermal conductivity and viscosity shows the higher value of the performance index. Therefore, single-particle and hybrid nanofluids with OS-shaped nanoparticles show the highest values of the performance index among all nanoparticle shapes and water. The performance index values of single-particle and hybrid nanofluids with PL-shaped nanoparticles are lowest among all nanoparticle shapes, as well as water, due to poor thermal conductivity and viscosity. Despite the lower heat transfer rate in OS-shaped nanoparticles, the lowest pressure drop results in the highest performance index. Whereas, the higher pressure drop for PL-shaped nanoparticles results

in the lowest performance index. Vo et al. have also illustrated that the pressure drop of PL-shaped nanoparticles is superior to other nanoparticle shapes, which increases as the volume fraction increases [20]. The OS- and PL-shaped nanoparticles show the maximum and minimum performance indexes for the alumina nanofluid, as proven by Bahiraei et al. and Arani et al. [19,53]. The single-particle and hybrid nanofluids with CY-shaped nanoparticles and the single-particle nanofluids with BL-shaped nanoparticles show a lower performance index than water despite better thermal conductivity because of higher viscosity and density. Apart from these combinations, other nanoparticle shapes present better performance index than water, in which hybrid nanofluids show a superior performance index than the single-particle nanofluid. The Al_2O_3 and $\text{Al}_2\text{O}_3/\text{Cu}$ nanofluids with OS-shaped nanoparticles present the performance index as higher by 2.24% and 6.58%, respectively, and those with PL-shaped nanoparticles present the performance index as lower by 8.78% and 5.80%, respectively, than water. The single-particle and hybrid nanofluids with other nanoparticle shapes show the performance index values in a range between the highest and lowest values.

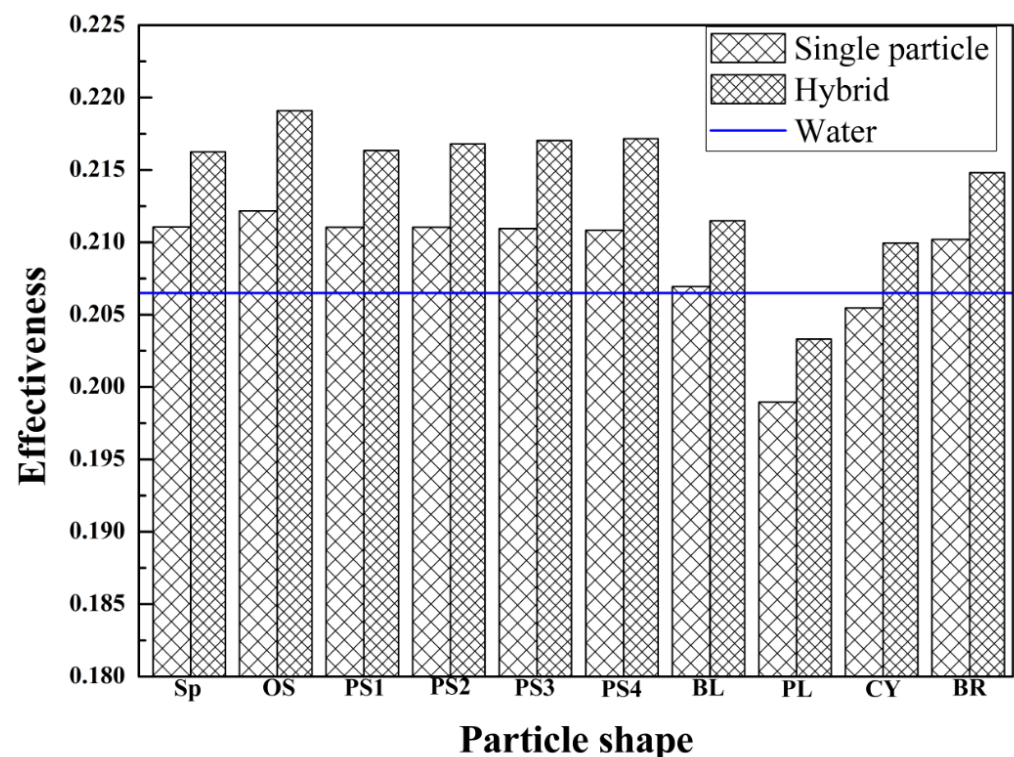


Figure 7. Effectiveness of single-particle and hybrid nanofluids with different nanoparticle shapes.

5.4. Evaluation of Second Law Characteristics for Different Nanoparticle Shapes

The thermal entropy generation rate for single-particle and hybrid nanofluids with different nanoparticle shapes is depicted in Figure 9. The thermal entropy generation is due to heat transfer, which depends on the temperature gradient. The thermal entropy generation rates of the hybrid nanofluid are better than that of single-particle nanofluids for OS-, PS2-, PS3- and PS4-shaped nanoparticles due to superior heat transfer properties and temperature gradients. However, in the case of Sp-, PS1-, BL-, PL-, CY- and BR-shaped nanoparticles, the thermal entropy generation rates of hybrid nanofluids are lower than single-particle nanofluids. The thermal entropy generation rates of all nanoparticle shapes except OS-shaped nanoparticles are lower than the water for both single-particle and hybrid nanofluids. The thermal entropy generation rates of single-particle and hybrid nanofluids with PL-shaped nanoparticles are lowest among all nanoparticle shapes. The PL-shaped nanoparticles have a higher velocity, which creates significant mixing and disturbance in the boundary layer. Hence, the temperature gradient decreases, which

results in a lower heat transfer and thermal entropy generation. The opposite discussion could be applied for OS-shaped nanoparticles with lower velocity. Bahiraei et al. have also presented that the thermal entropy generation rates are highest and lowest for OS- and PL-shaped nanoparticles, respectively [13,48]. The Al_2O_3 and $\text{Al}_2\text{O}_3/\text{Cu}$ nanofluids with OS-shaped nanoparticles show thermal entropy generation rates as higher by 0.14% and 0.70%, respectively, compared to water; however, the percentage increase is not significantly higher. The thermal entropy generation rates of Al_2O_3 and $\text{Al}_2\text{O}_3/\text{Cu}$ nanofluids with PL-shaped nanoparticles are lower by 6.08% and 6.53%, respectively, compared to water.

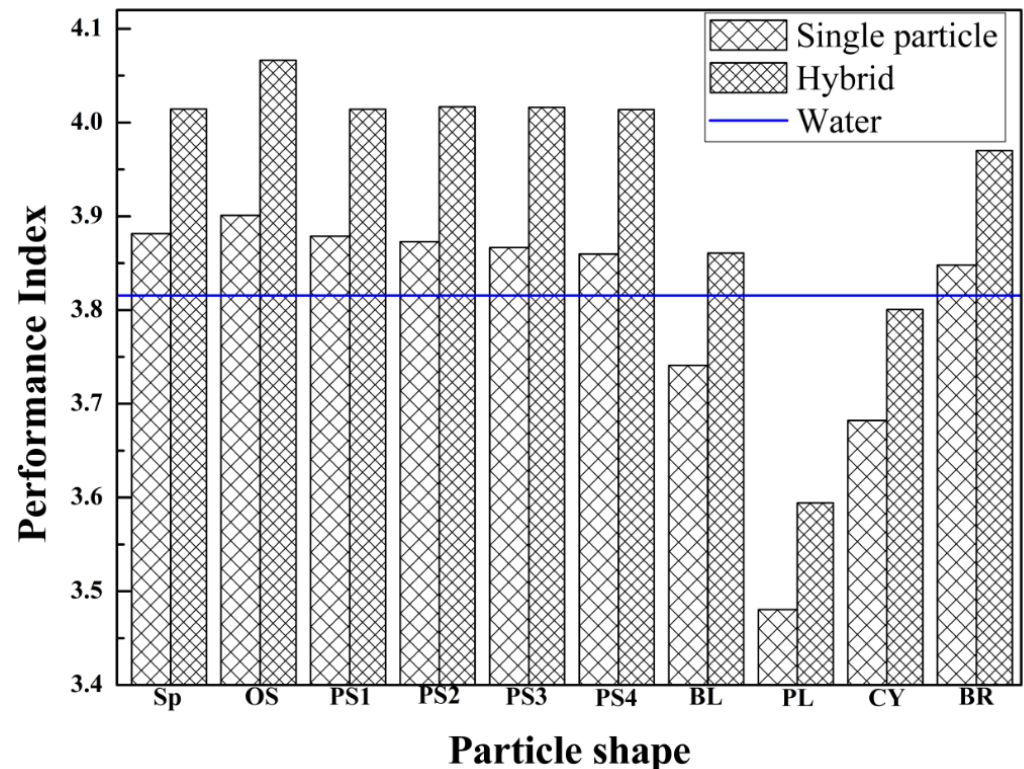


Figure 8. Comparison of performance index of single-particle and hybrid nanofluids with different particle shapes.

The comparison of the friction entropy generation rate for single-particle and hybrid nanofluids with different nanoparticle shapes is shown in Figure 10. The friction entropy generation is due to a pressure drop, which depends on the density and viscosity of nanofluids with various nanoparticle shapes. The friction entropy generation rates are lower for hybrid nanofluids compared to single-particle nanofluids for all nanoparticle shapes. Except for single-particle nanofluids with PL- and CY-shaped nanoparticles, the friction entropy generation rates of other combinations are lower than water. The single-particle and hybrid nanofluids with Sp- and OS-shaped nanoparticles present the lowest and second lowest values of friction entropy generation rates because of the same order of viscosity behavior for both nanoparticle shapes. The single-particle and hybrid nanofluids with PL-shaped nanoparticles show the highest values of friction entropy generation rates due to superior values of viscosity among all nanoparticles. The higher and lower values of friction entropy generation rates correspond to higher and lower velocity gradients of different nanoparticle shapes. Mahian et al. have also shown a trend in similar results, in that the friction entropy generation rate for PL-shaped nanoparticles is superior, followed by CY-, BL- and BR-shaped nanoparticles in the decreasing order [11]. The friction entropy generation rates of Al_2O_3 and $\text{Al}_2\text{O}_3/\text{Cu}$ nanofluids with Sp-shaped nanoparticles are lower by 1.93% and 5.13%, respectively, and those with OS-shaped nanoparticles are lower by 1.91% and 5.11%, respectively, than water. The friction entropy generation rate of the

Al_2O_3 nanofluid with PL-shaped nanoparticles is higher by 2.73% and that of the $\text{Al}_2\text{O}_3/\text{Cu}$ nanofluid with PL-shaped nanoparticles are lower by 0.74% compared to water.

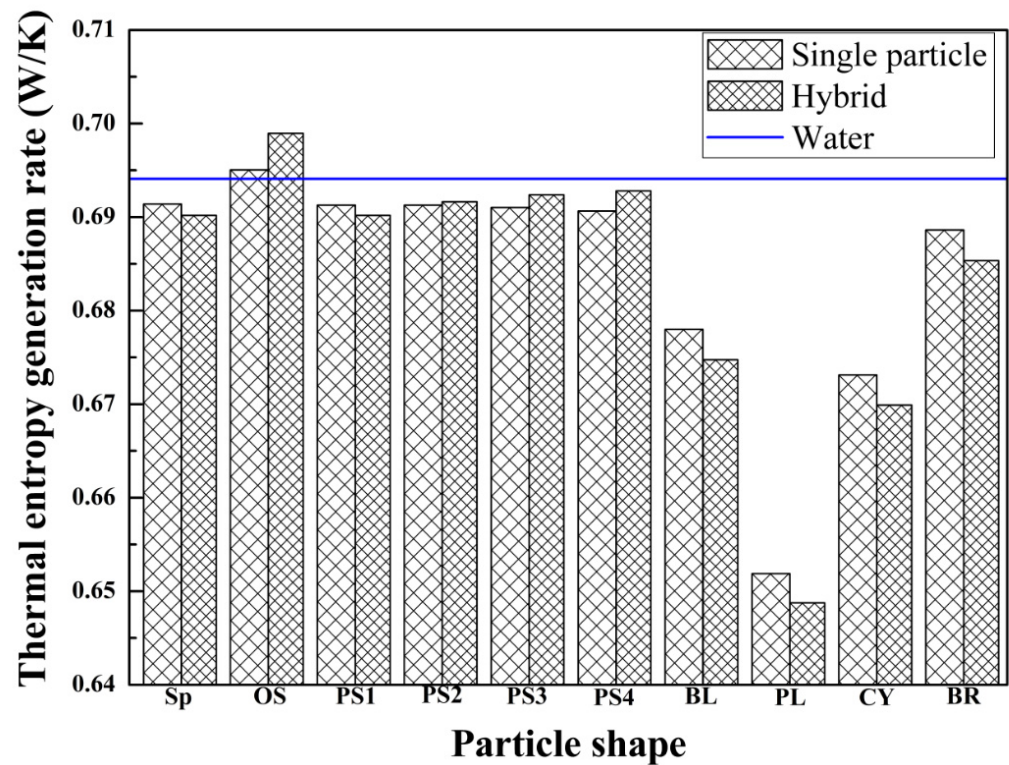


Figure 9. Thermal entropy generation rate for single-particle and hybrid nanofluids with different nanoparticle shapes.

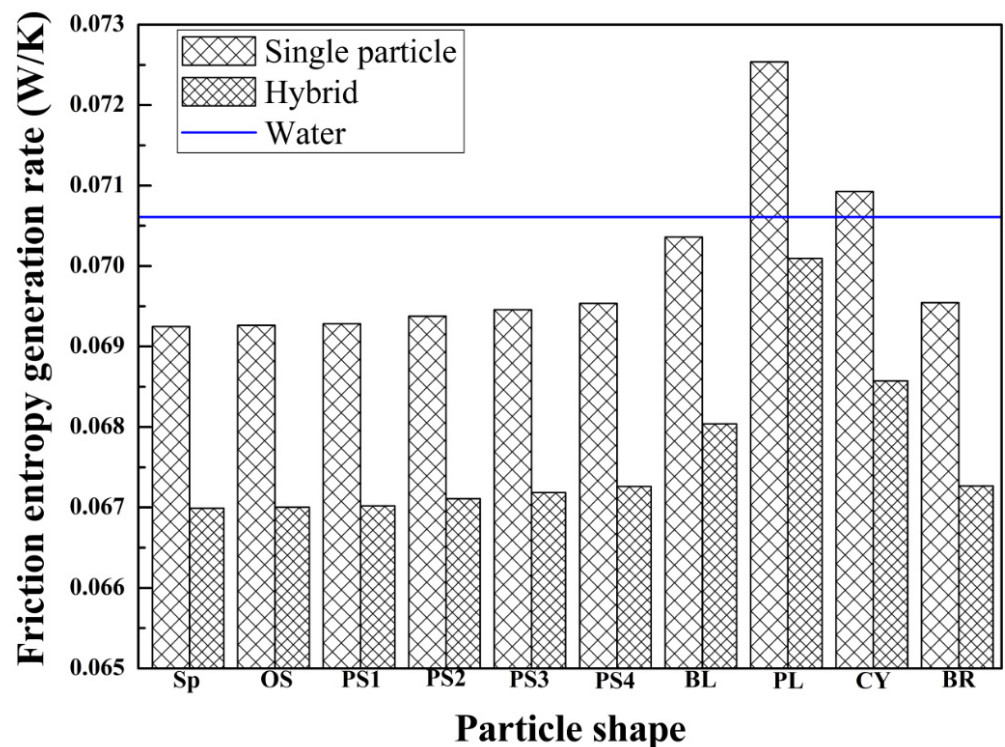


Figure 10. Comparison of friction entropy generation rate for single-particle and hybrid nanofluids with different nanoparticle shapes.

The behavior of the Bejan number for single-particle and hybrid nanofluids with different nanoparticle shapes is depicted in Figure 11. The Bejan number presents the contribution of thermal entropy generation in total entropy generation. The Bejan numbers of hybrid nanofluids are superior to single-particle nanofluids for all nanoparticle shapes. In addition, except the single-particle and hybrid nanofluids with PL- and CY-shaped nanoparticles and single-particle nanofluids with BL-shaped nanoparticles, all other combinations present higher values of Bejan numbers compared to water. The OS-shaped nanoparticles show the highest values of Bejan numbers, followed by Sp, PS1, PS2, PS3, PS4, BR, BL, CY and PL, respectively, in the decreasing order of the Bejan number for single-particle nanofluids. In the case of hybrid nanofluids, the decreasing order of Bejan numbers are OS-, PS2 = PS3-, Sp-, PS4-, PS1-, BR-, BL-, CY- and PL-shaped nanoparticles, respectively. The OS-shaped nanoparticles show a higher contribution of the thermal entropy generation rate and a lower contribution of the friction entropy generation rate, which results in the highest value of the Bejan number. The opposite discussion could be applied for PL-shaped nanoparticles for the lowest value of the Bejan number. Al-Rashed et al. and Monfared et al. have also shown the lower Bejan number for PL-shaped nanoparticles [28,29]. The Bejan number is maximum for OS-shaped nanoparticles and minimum for PL-shaped nanoparticles, as presented by Bahiraei et al. [48]. Compared to water, the Al_2O_3 and $\text{Al}_2\text{O}_3/\text{Cu}$ nanofluids with OS-shaped nanoparticles depict the Bejan number as higher by 0.19% and 0.54%, respectively, and those with PL-shaped nanoparticles depict the Bejan number as lower by 0.86% and 0.57%, respectively.

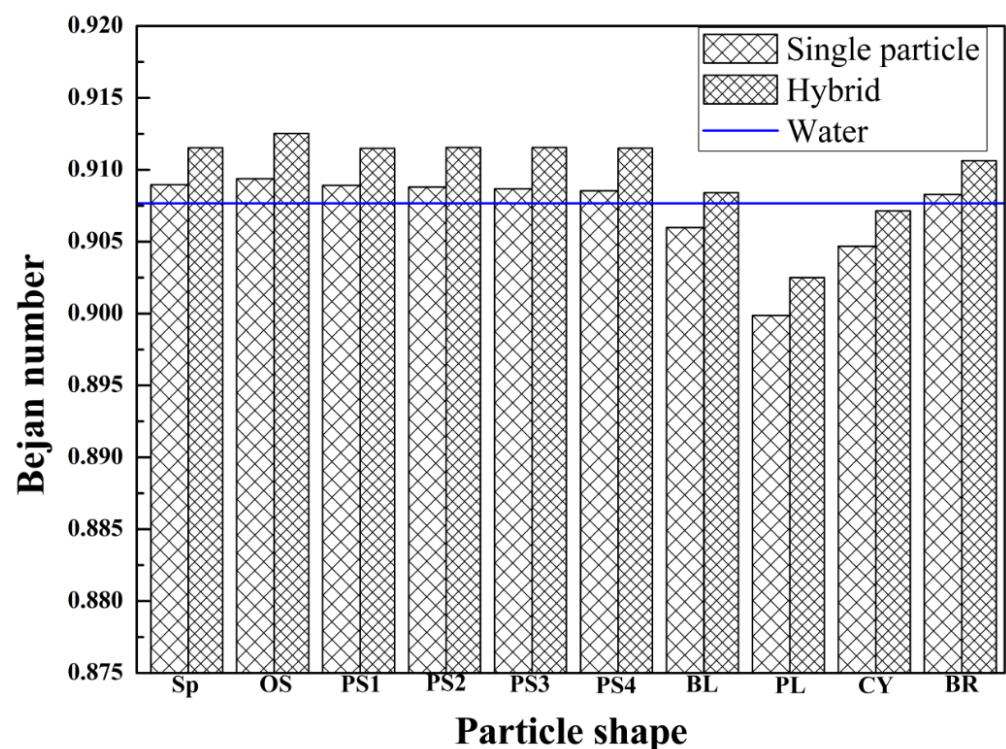


Figure 11. The behavior of Bejan number for single-particle and hybrid nanofluids with different nanoparticle shapes.

The combination of hybrid nanofluid with OS shaped nanoparticles show the excellent first law and second law characteristics compared to other combinations as well as water. Therefore, the first law characteristic namely, performance index and the second law characteristic namely, Bejan number of hybrid nanofluid ($\text{Al}_2\text{O}_3/\text{Cu}$) with OS shaped nanoparticles are further investigated for different temperatures and mass flow rates of hot and cold fluids. In addition, the influence of volume fraction is also integrated while investigating the effect of temperature and mass flow rate on different characteristics. The

performance index presents the combined effect of heat transfer and pressure drop whereas, the Bejan number presents the combined effect of thermal and friction entropy generations hence, these two parameters are considered as the first and second law characteristics under the influence of various boundary parameters.

5.5. Effect of Hot Fluid Temperature on First and Second Law Characteristics

The behavior of first and second law characteristics of the $\text{Al}_2\text{O}_3/\text{Cu}$ nanofluid with OS-shaped nanoparticles for various volume fractions and hot fluid temperatures is presented in Figure 12. The hot fluid temperature varies at 90 °C, 80 °C, and 70 °C and the volume fraction varies at 0.5%, 1.0% and 2.0%. The performance index increases with an increase in the volume fraction as well as hot fluid temperature. The heat transfer and pressure drop both increase with an increase in volume fraction, but the increase in the heat transfer dominates compared to the increase in the pressure drop, hence, as a result, the performance index increases as the volume fraction increases for all hot fluid temperatures. The hot fluid at the higher temperature could transfer more heat compared to hot fluid at a lower temperature. The pressure drop remains almost the same for various hot fluid temperatures, whereas the heat transfer increases with a rise in the temperature, which shows an enhancement in the performance index with an increase in the hot fluid temperature for all volume fractions. The performance index of $\text{Al}_2\text{O}_3/\text{Cu}$ with OS-shaped nanoparticles increases by 20% and 40% as the hot fluid temperature increases from 70 °C to 80 °C and 70 °C to 90 °C, respectively, for each volume fraction. With the increase in volume fraction from 0.5% to 2.0%, the performance index of $\text{Al}_2\text{O}_3/\text{Cu}$ with OS-shaped nanoparticles enhances by 9.42% for each hot fluid temperature. As elaborated, the heat transfer enhances with an increase in the volume fraction and hot fluid temperature due to an increase in the temperature gradient. Hence, the thermal entropy generation rate increases with an increase in the volume fraction and hot fluid temperature. The increase in the thermal entropy generation rate with the volume fraction is not significantly high, but could not be neglected. The friction entropy generation depends on the pressure drop, but as per the formula, the friction entropy generation rate is evaluated based on the ratio of pressure drop and average temperature. The pressure drop and average temperature both increase as the volume fraction increases, but as explained before, the dominance of the heat transfer is more than pressure drop with an increase in the volume fraction, which leads to a higher increase rate of average temperature than the pressure drop. Therefore, the friction entropy generation rate decreases as the volume fraction increases for all hot fluid temperatures. The pressure drop shows negligible change and heat transfer shows significant enhancement with a rise in the hot fluid temperature. Therefore, the dominance of average temperature rise is higher than the pressure drop as the hot fluid temperature increases, which results in a decrease in the friction entropy generation rate with an increase in the hot fluid temperature for all volume fractions. The Bejan number increases with an increase in the volume fraction and an increase in the hot fluid temperature, because the thermal entropy generation rate increases and the friction entropy generation rate decreases as the volume fraction and hot fluid temperature have increased. The Bejan number is at maximum at the higher hot fluid temperature and higher volume fraction. The Bejan number of $\text{Al}_2\text{O}_3/\text{Cu}$ with OS-shaped nanoparticles increases by 2.12%, 2.06% and 1.95% as the hot fluid temperature increases from 70 °C to 80 °C, and that increases by 3.69%, 3.58% and 3.40% when the hot fluid temperature increases from 70 °C to 90 °C for volume fractions of 0.5%, 1.0% and 2.0%, respectively. As the volume fraction increases from 0.5% to 2.0%, the Bejan number of $\text{Al}_2\text{O}_3/\text{Cu}$ with OS-shaped nanoparticles increases by 1.01%, 0.85% and 0.73% for hot fluid temperatures of 70 °C, 80 °C, and 90 °C, respectively. Singh and Sarkar have presented the improvement in Nusselt number and reduction in friction factor with an increase in hot fluid temperature [62]. The contributions of thermal and friction entropy generation rates for $\text{Al}_2\text{O}_3/\text{Cu}$ with OS-shaped nanoparticles at various hot fluid temperatures are depicted in Figure 13.

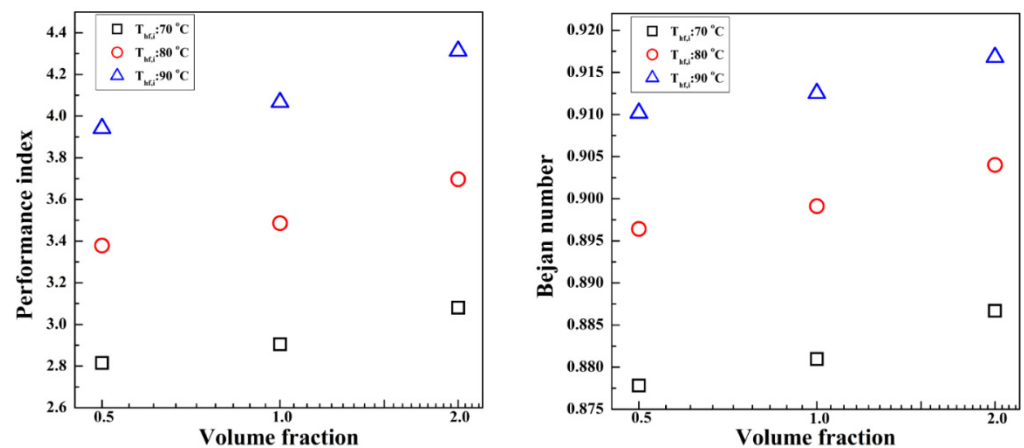


Figure 12. Behavior of first and second law characteristics of $\text{Al}_2\text{O}_3/\text{Cu}$ nanofluid with OS-shaped nanoparticles for various volume fractions and hot fluid temperatures.

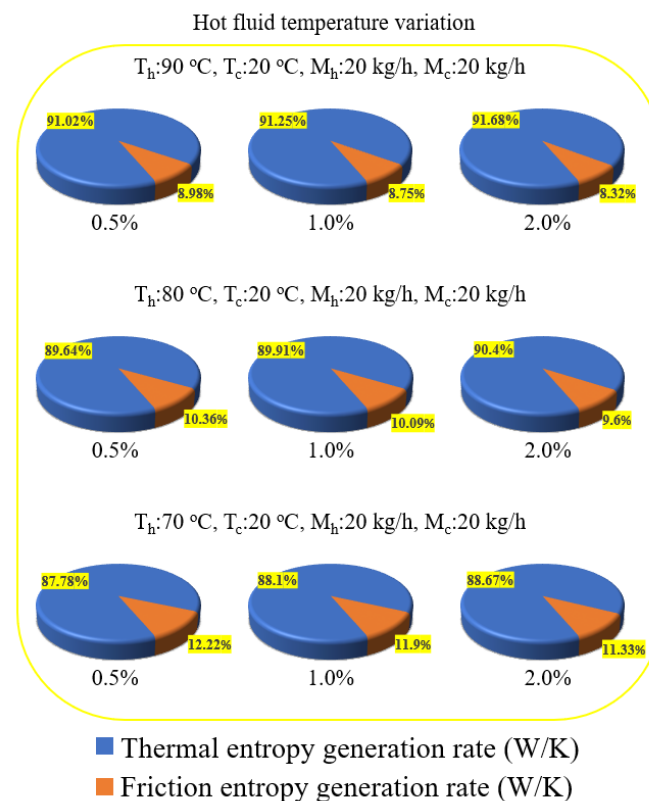


Figure 13. Contributions of thermal and friction entropy generation rates for $\text{Al}_2\text{O}_3/\text{Cu}$ with OS-shaped nanoparticles at various hot fluid temperatures.

5.6. Effect of Hot Fluid Mass Flow Rate on First and Second Law Characteristics

The effect of the hot fluid mass flow rate and volume fraction on first and second law characteristics of hybrid nanofluids with OS-shaped nanoparticles is presented in Figure 14. The hot fluid mass flow rate varies at 10 kg/h, 20 kg/h and 30 kg/h. The performance index increases with the volume fraction for the same hot fluid mass flow rate because of higher dominance of the heat transfer increase compared to the pumping power increase as the volume fraction increases. Moreover, the steepness of the increasing trend of the performance index with the volume fraction becomes sharp at the higher hot fluid mass flow rate. For the same volume fraction, the performance index decreases with an increase in the hot fluid mass flow rate because the dominance of the increase in the pumping power is superior compared to the increase in heat transfer with an increase in the hot

fluid mass flow rate. The performance index of $\text{Al}_2\text{O}_3/\text{Cu}$ with OS-shaped nanoparticles increases by 3.99%, 9.43% and 12.27% for hot fluid mass flow rates of 10 kg/h, 20 kg/h and 30 kg/h, respectively, as the volume fraction increases from 0.5% to 2.0%. The performance index of $\text{Al}_2\text{O}_3/\text{Cu}$ with OS-shaped nanoparticles decreases by 39.37%, 38.29% and 36.20% as the hot fluid mass flow rate increases from 10 kg/h to 20 kg/h, and that decreases by 70.31%, 69.51% and 67.94% as the hot fluid mass flow rate increases from 10 kg/h to 30 kg/h for volume fractions of 0.5%, 1.0% and 2.0%, respectively. The thermal entropy generation rate increases with an increase in the hot fluid mass flow rate for all volume fractions, due to increase in the temperature gradient and heat transfer. Similarly, the heat transfer enhances with the volume fraction, which results in an increase in the thermal entropy generation rate with an increase in the volume fraction for all hot fluid mass flow rates. However, the increasing trends of thermal entropy generation rates with volume fractions are not steep for higher hot fluid mass flow rates. The pressure drop and average temperature have both increased with an increase in volume fraction and hot fluid mass flow rate. With an increase in volume fraction, the increase in average temperature is more dominant than the increase in pressure drop, hence the friction entropy generation rate decreases as the volume fraction increases for all hot fluid mass flow rates. This decreasing trend becomes steeper with the volume fraction at the higher mass flow rates. On the other side, with the increase in the hot fluid mass flow rate, the increase in the pressure drop is dominating compared to the increase in average temperature; therefore, the friction entropy generation rate is high at a higher mass flow rate and vice versa for all volume fractions. Based on the trends for the thermal and friction entropy generation rates with volume fractions and hot fluid mass flow rate, the Bejan number is evaluated. The Bejan number increases with the increase in volume fraction and decrease in the hot fluid mass flow rate. The thermal entropy generation increases, and the friction entropy generation decreases with the increase in volume fraction, which results in an increase in the Bejan number with an increase in the volume fraction. The thermal and friction entropy generation rates have both increased with the increase in the hot fluid mass flow rate but the increasing rate of the friction entropy generation rate is significantly higher than the thermal entropy generation rate. Therefore, the Bejan number decreases with the increase in the hot fluid mass flow rate for each volume fraction. The Bejan number of the $\text{Al}_2\text{O}_3/\text{Cu}$ nanofluid with OS-shaped nanoparticles increases by 0.21%, 0.73% and 1.74% for hot fluid mass flow rates of 10 kg/h, 20 kg/h and 30 kg/h, respectively, as the volume fraction increases from 0.5% to 2.0%. The Bejan number of $\text{Al}_2\text{O}_3/\text{Cu}$ with OS-shaped nanoparticles decreases by 3.06%, 2.89% and 2.57% as the hot fluid mass flow rate increases from 10 kg/h to 20 kg/h, and that decreases by 10.72%, 10.24% and 9.37% as the hot fluid mass flow rate increases from 10 kg/h to 30 kg/h for volume fractions of 0.5%, 1.0% and 2.0%, respectively. Soroush and Chamkha have also shown that the first and second law characteristics of single-particle nanofluids enhances as the volume fraction increases for all nanoparticle shapes [30]. The contributions of thermal and friction entropy generation rates for $\text{Al}_2\text{O}_3/\text{Cu}$ with OS-shaped nanoparticles at various hot fluid mass flow rates are depicted in Figure 15.

5.7. Effect of Cold Fluid Temperature on First and Second Law Characteristics

The variation in first and second law characteristics of hybrid nanofluid with OS-shaped nanoparticles for various volume fractions and cold fluid temperatures is depicted in Figure 16. The cold fluid temperature is varied as 10 °C, 20 °C and 30 °C. The cold fluid at the lower temperature absorbs more heat and presents the higher temperature gradient and heat transfer rate. The pressure drop is not significantly affected by change in the cold fluid temperature. Therefore, the performance index increases as the cold fluid temperature decreases. With the increase in volume fraction, the dominance of the increase in heat transfer is superior to the increase in the pressure drop; therefore, the performance index increases with the increase in the volume fraction. The performance index of the $\text{Al}_2\text{O}_3/\text{Cu}$ nanofluid with OS-shaped nanoparticles decreases by 12.5% and 24.99% when

the cold fluid temperature increases from 10 °C to 20 °C and 10 °C to 30 °C, respectively, for all volume fractions. With an increase in the volume fraction from 0.5% to 2.0%, the performance index increases by 9.43% for all cold fluid temperatures. The thermal entropy generation increases with the increase in volume fraction and decrease in the cold fluid temperature because the heat transfer rate increases with the increase in volume fraction and decrease in the cold fluid temperature. The friction entropy generation rate decreases with the increase in volume fraction despite an increase in pressure drop, because the increase in the average temperature with an increase in the volume fraction is dominant compared to an increase in pressure drop. Similar to the hot fluid temperature, the lower cold fluid temperature presents higher values of the friction entropy generation rate, and vice versa. The higher Bejan number is obtained at the lower cold fluid temperature because the dominance of the thermal entropy generation increase is higher than the friction entropy generation increase with a decrease in the cold fluid temperature. The thermal entropy generation increases and the friction entropy generation decreases with an increase in the volume fraction, which results in an increase in the Bejan number. The Bejan number of the $\text{Al}_2\text{O}_3/\text{Cu}$ nanofluid with OS-shaped nanoparticles decreases by 1.16%, 1.12% and 1.07% as the cold fluid temperature increases from 10 °C to 20 °C, and that decreases by 2.66%, 2.59% and 2.45% as the cold fluid temperature increases from 10 °C to 30 °C for volume fractions of 0.5%, 1.0% and 2.0%, respectively. With the increase in volume fraction from 0.5% to 2.0%, the Bejan number of $\text{Al}_2\text{O}_3/\text{Cu}$ nanofluid with OS-shaped nanoparticles increases by 0.63%, 0.73% and 0.85% for cold fluid temperatures of 10 °C, 20 °C and 30 °C, respectively. Garud et al. have proved that the performance of the heat exchanger is optimum for the lower mass flow rate of cold fluid [66]. The contributions of thermal and friction entropy generation rates for $\text{Al}_2\text{O}_3/\text{Cu}$ with OS-shaped nanoparticles at various cold fluid temperatures are depicted in Figure 17.

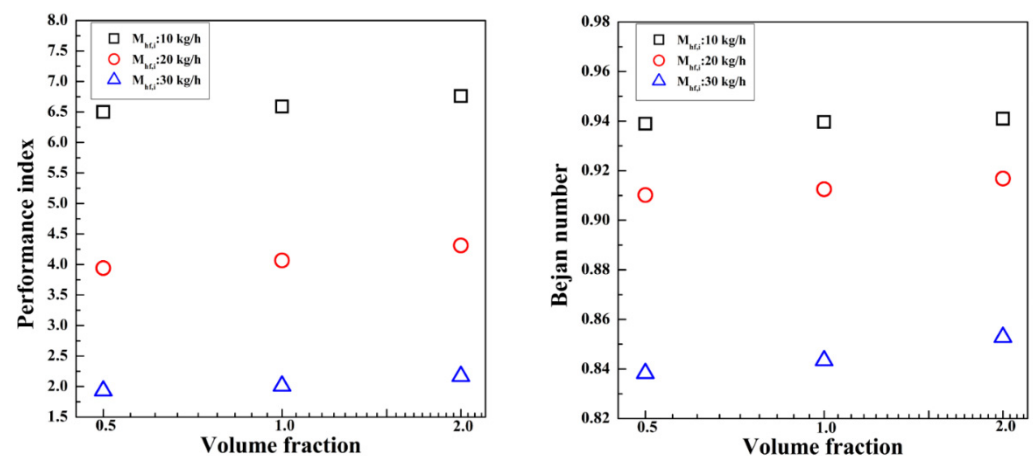


Figure 14. Effect of hot fluid mass flow rate and volume fraction on first and second law characteristics of hybrid nanofluid with OS-shaped nanoparticles.

5.8. Effect of Cold Fluid Mass Flow Rate on First and Second Law Characteristics

The behavior of first and second law characteristics of the hybrid nanofluid with OS-shaped nanoparticles for various volume fractions and cold fluid mass flow rates is presented in Figure 18. The cold fluid mass flow rate is varied at 10 kg/h, 20 kg/h and 30 kg/h. The ratio of heat transfer to pumping power is dominating at a higher volume fraction and lower cold fluid mass flow rate. Therefore, the performance index increases with the increase in volume fraction and decrease in cold fluid mass flow rate. The performance index of the $\text{Al}_2\text{O}_3/\text{Cu}$ nanofluid with OS-shaped nanoparticles increases by 13.41%, 9.43% and 5.79% for cold fluid mass flow rates of 10 kg/h, 20 kg/h and 30 kg/h, respectively, as the volume fraction increases from 0.5% to 2.0%. The performance index of the $\text{Al}_2\text{O}_3/\text{Cu}$ nanofluid with OS-shaped nanoparticles decreases by 6.41%, 7.52% and 9.70% as the cold fluid mass flow rate increases from 10 kg/h to 20 kg/h, and that decreases

by 38.71%, 40.13% and 42.82% as the cold fluid mass flow rate increases from 10 kg/h to 30 kg/h for volume fractions of 0.5%, 1.0% and 2.0%, respectively. The thermal entropy generation rate increases with the volume fraction and cold fluid mass flow rate due to an increase in the heat transfer at a higher volume fraction and higher cold fluid mass rate. For the same cold fluid mass flow rate, the ratio of pressure drop to average temperature is less dominant at a higher volume fraction; therefore, the friction entropy generation rate decreases with an increase in volume fraction. The friction entropy generation increases with an increase in the cold fluid mass flow rate for all volume fractions because the ratio of pressure drop to average temperature is highly dominant at higher cold fluid mass flow rates. The ratio of thermal entropy generation rate to total entropy generation rate presents an increasing trend of Bejan numbers with an increase in volume fraction and a decrease in the cold fluid mass flow rate. With the increase in volume fraction from 0.5% to 2.0%, the Bejan number of the Al₂O₃/Cu nanofluid with OS-shaped nanoparticles increases by 0.94%, 0.73% and 0.69% for cold fluid mass flow rates of 10 kg/h, 20 kg/h and 30 kg/h, respectively. The Bejan number of the Al₂O₃/Cu nanofluid with OS-shaped nanoparticles decreases by 1.06%, 1.13% and 1.26% as the cold fluid mass flow rate increases from 10 kg/h to 20 kg/h, and that decreases by 6.21%, 6.30% and 6.45% as the cold fluid mass flow rate increases from 10 kg/h to 30 kg/h for volume fractions of 0.5%, 1.0% and 2.0%, respectively. Tiwari et al. have proved that the lower cold fluid mass flow rate shows the better first law characteristics compared to the higher cold fluid mass flow rate [59,61]. The contributions of thermal and friction entropy generation rates for Al₂O₃/Cu with OS-shaped nanoparticles at various cold fluid mass flow rates are depicted in Figure 19.

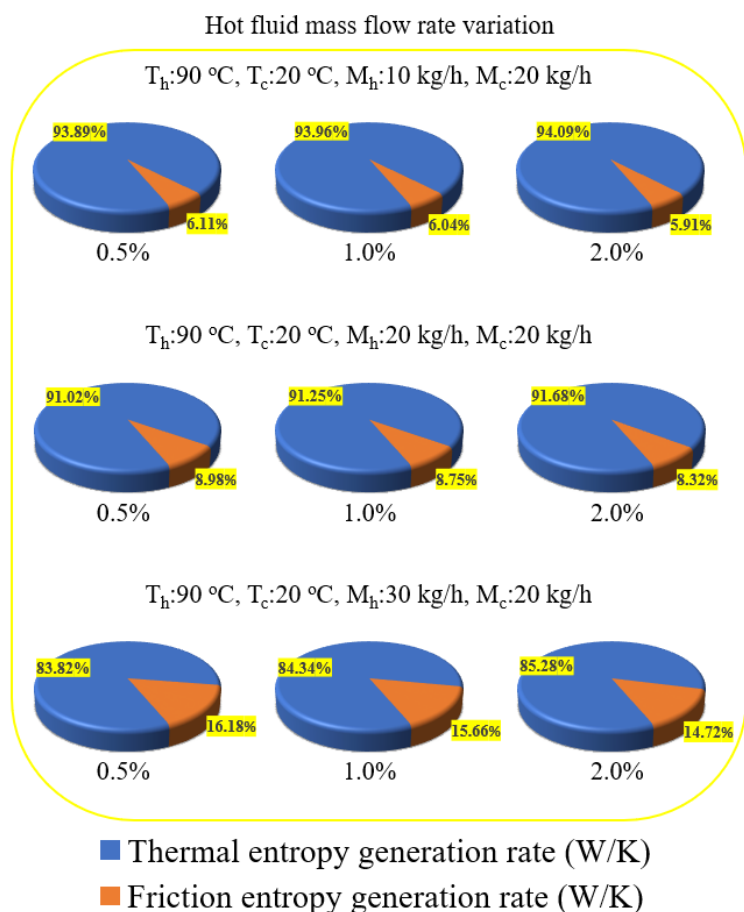


Figure 15. Contributions of thermal and friction entropy generation rates for Al₂O₃/Cu with OS-shaped nanoparticles at various hot fluid mass flow rates.

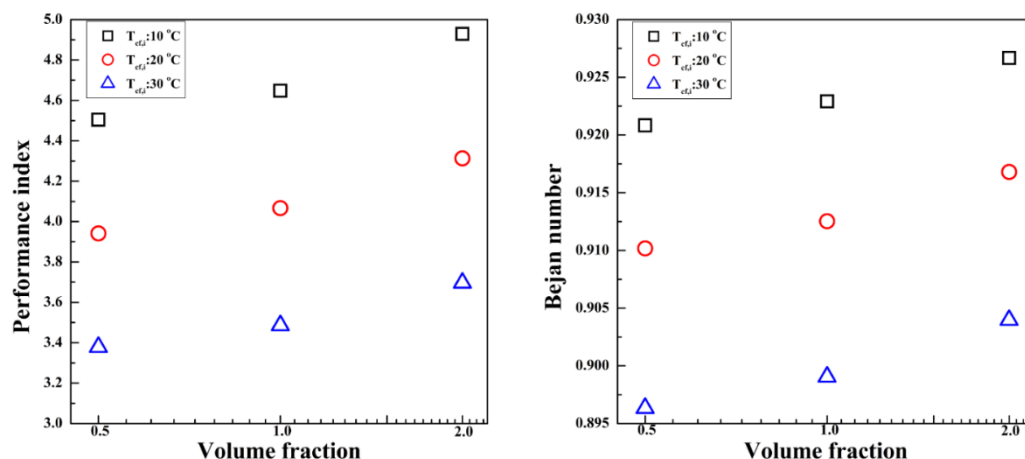


Figure 16. Variation in first and second law characteristics of hybrid nanofluid with OS-shaped nanoparticles with various volume fractions and cold fluid temperatures.

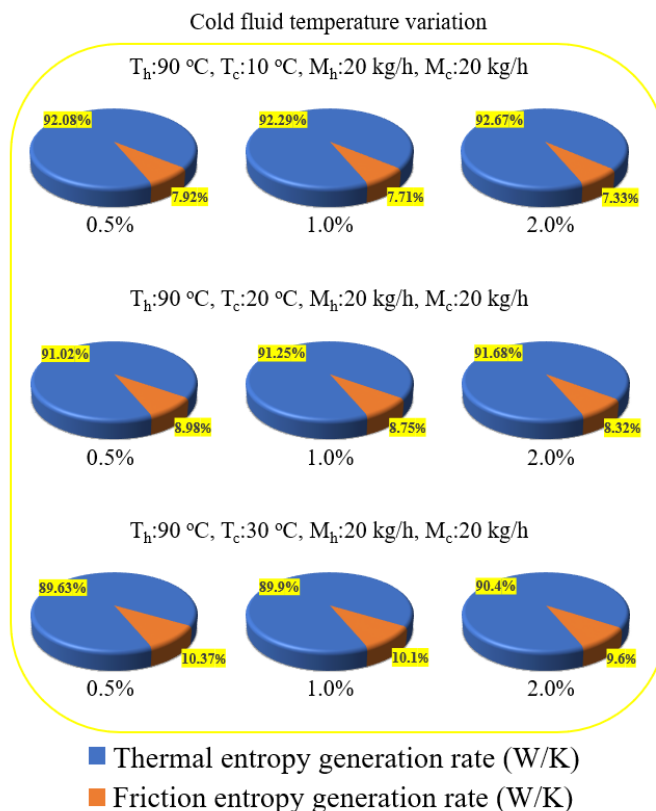


Figure 17. Contributions of thermal and friction entropy generation rates for $\text{Al}_2\text{O}_3/\text{Cu}$ with OS-shaped nanoparticles at various cold fluid temperatures.

The above-mentioned results in Sections 5.3–5.8 are summarized as the comparison of single-particle and hybrid nanofluids with different nanoparticle shapes, based on numerous first and second law characteristics of the microplate heat exchanger. The $\text{Al}_2\text{O}_3/\text{Cu}$ nanofluid with OS-shaped nanoparticles presents the excellent first and second law characteristics among all combinations of single-particle and hybrid nanofluids with nanoparticle shapes. The first and second law characteristics in terms of performance index and Bejan number are investigated under various conditions of volume fraction, temperature and mass flow rate for the best combination of $\text{Al}_2\text{O}_3/\text{Cu}$ nanofluid with OS-shaped nanoparticles. The performance index and Bejan number of the $\text{Al}_2\text{O}_3/\text{Cu}$

nanofluid with OS-shaped nanoparticles are maximum at a higher hot fluid temperature, lower cold fluid temperature and lower mass flow rates of hot and cold fluids.

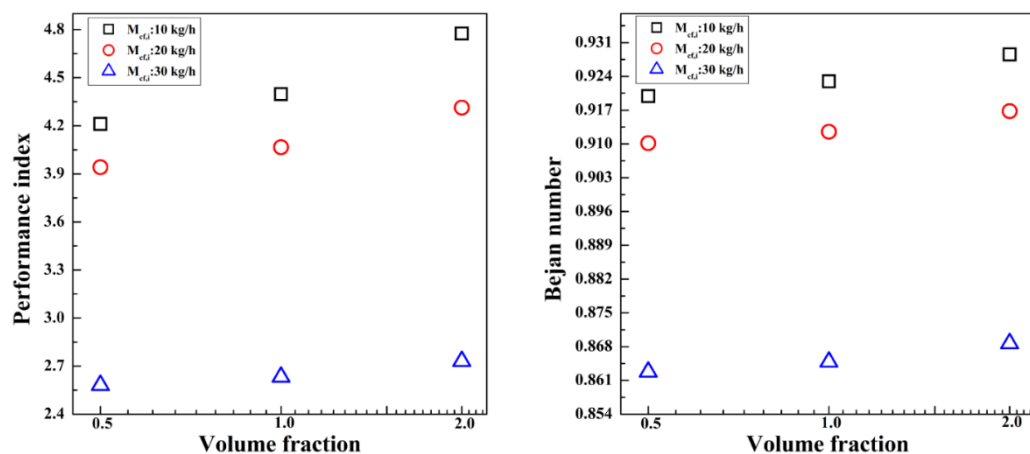


Figure 18. Behavior of first and second law characteristics of hybrid nanofluid with OS-shaped nanoparticles for various volume fractions and cold fluid mass flow rates.

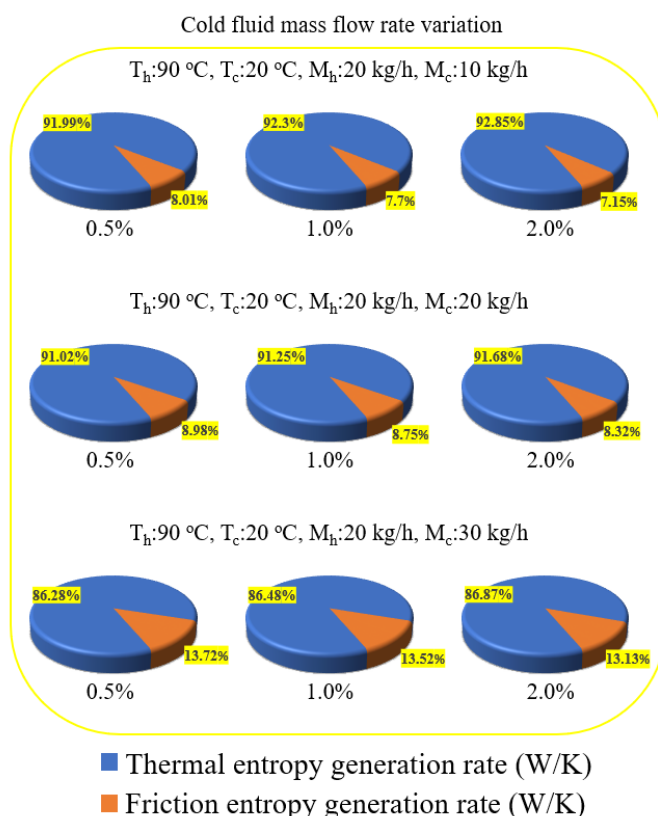


Figure 19. Contributions of thermal and friction entropy generation rates for $\text{Al}_2\text{O}_3/\text{Cu}$ with OS-shaped nanoparticles at various cold fluid mass flow rates.

6. Conclusions

The first and second law analyses have been conducted on the microplate heat exchanger, comprising of single-particle and hybrid nanofluids with different-shaped nanoparticles. Firstly, the first and second law characteristics are compared for different-shaped nanoparticles, and then the effect of various volume fractions, temperatures and mass flow rates are investigated on the first and second law characteristics of the optimum-shaped nanoparticles. The following key findings are highlighted from the present study.

- (a) The decreasing order of first law characteristics is evaluated as hybrid nanofluid, single-particle nanofluid and water, respectively, for all nanoparticle shapes. The $\text{Al}_2\text{O}_3/\text{Cu}$ nanofluid with OS-shaped nanoparticles shows maximum values of NTU, effectiveness and performance index, which are higher by 6.38%, 6.10% and 6.58%, respectively, compared to water. The Al_2O_3 nanofluid with PL-shaped nanoparticles shows minimum values of NTU, effectiveness and performance index, which are lower by 3.99%, 3.65% and 8.78%, respectively, compared to water. The $\text{Al}_2\text{O}_3/\text{Cu}$ nanofluid with OS-shaped nanoparticles shows the optimum values of first law characteristics.
- (b) The thermal entropy generation rates of OS-shaped nanoparticles are at a maximum, which are 0.14% and 0.70% higher for Al_2O_3 and $\text{Al}_2\text{O}_3/\text{Cu}$ nanofluids, respectively, compared to water. The friction entropy generation rates are maximum for PL-shaped nanoparticles which are 2.73% higher and 0.74% lower for Al_2O_3 and $\text{Al}_2\text{O}_3/\text{Cu}$ nanofluids, respectively, compared to water. The increasing order of Bejan numbers are water, single-particle nanofluid and hybrid nanofluid, respectively, for all nanoparticle shapes. The Bejan number of the $\text{Al}_2\text{O}_3/\text{Cu}$ nanofluid with OS-shaped nanoparticles is the maximum, and that of the Al_2O_3 nanofluid with PL-shaped nanoparticles is the minimum, which are 0.54% higher and 0.86% lower compared to water. The $\text{Al}_2\text{O}_3/\text{Cu}$ nanofluid with OS-shaped nanoparticles shows the optimum values of second law characteristics.
- (c) The first law characteristic performance index of the $\text{Al}_2\text{O}_3/\text{Cu}$ nanofluid with OS-shaped nanoparticles has increased with an increase in volume fraction for various temperature and mass flow rate conditions of hot and cold fluids. The performance index increases with the increase in the hot fluid temperature and decrease in the cold fluid temperature for all volume fractions. The performance index has decreased with the increase in the hot and cold fluid mass flow rates.
- (d) The second law characteristic Bejan number of the $\text{Al}_2\text{O}_3/\text{Cu}$ nanofluid with OS-shaped nanoparticles has increased with the increase in the volume fraction for all temperature and mass flow rate conditions of hot and cold fluids. The Bejan number has increased with the increase in hot fluid temperature, whereas with the increase in the cold fluid temperature, the Bejan number has decreased for all volume fractions. The Bejan number has decreased with the increase in hot and cold fluid mass flow rates for all volume fractions.

Author Contributions: Conceptualization, K.S.G.; and M.-Y.L.; methodology, K.S.G.; S.-G.H.; and M.-Y.L.; formal analysis, K.S.G.; S.-G.H.; and M.-Y.L.; investigation, K.S.G.; S.-G.H.; T.-K.L.; N.K.; and M.-Y.L.; resources, K.S.G.; and M.-Y.L.; data curation, K.S.G.; and T.-K.L.; validation, K.S.G.; software, K.S.G.; writing—original draft preparation, K.S.G.; and M.-Y.L.; writing—review and editing, K.S.G.; T.-K.L.; N.K.; and M.-Y.L.; visualization, K.S.G.; and M.-Y.L.; supervision, M.-Y.L.; project administration, M.-Y.L.; funding acquisition, M.-Y.L. All authors have read and agreed to the published version of the manuscript.

Funding: This research received no external funding.

Institutional Review Board Statement: Not applicable.

Informed Consent Statement: Not applicable.

Data Availability Statement: The data presented in this study will be available on request to the corresponding author.

Acknowledgments: This work was supported by the Dong-A University research fund.

Conflicts of Interest: The authors declare no conflict of interest.

Nomenclature

A	total heat transfer area (m^2)
C_{cf}	cold fluid heat capacity (W/K)
C_{hf}	hot fluid heat capacity (W/K)
C_{min}	minimum heat capacity (W/K)
$C_{p,bf}$	specific heat of base fluid ($J/kg \cdot K$)
$C_{p,cf}$	cold fluid specific heat ($J/kg \cdot K$)
$C_{p,hf}$	hot fluid specific heat ($J/kg \cdot K$)
$C_{p,hnf}$	specific heat of hybrid nanofluid ($J/kg \cdot K$)
$C_{p,nf}$	specific heat of nanofluid ($J/kg \cdot K$)
$C_{p,np}$	specific heat of nanoparticles ($J/kg \cdot K$)
$C_{p,np1}$	specific heat of nanoparticle1 ($J/kg \cdot K$)
$C_{p,np2}$	specific heat of nanoparticle2 ($J/kg \cdot K$)
h	enthalpy (J/kg)
k	turbulent kinetic energy (J/kg)
k_{bf}	thermal conductivity of base fluid ($W/m \cdot K$)
k_{hnf}	thermal conductivity of hybrid nanofluid ($W/m \cdot K$)
k_{nf}	thermal conductivity of nanofluid ($W/m \cdot K$)
k_{np}	thermal conductivity of nanoparticle ($W/m \cdot K$)
k_{np1}	thermal conductivity of nanoparticle1 ($W/m \cdot K$)
k_{np2}	thermal conductivity of nanoparticle2 ($W/m \cdot K$)
\dot{m}_{cf}	cold fluid mass flow rate (kg/s)
\dot{m}_{hf}	hot fluid mass flow rate (kg/s)
m_{np}	mass of nanoparticles (kg)
p	static pressure (Pa)
Q_{max}	maximum possible heat transfer rate (W)
\dot{S}_{Fr}	Volumetric friction entropy generation rate ($W/m^3 \cdot K$)
\dot{S}_{Th}	Volumetric thermal entropy generation rate ($W/m^3 \cdot K$)
\dot{S}_T	Volumetric total entropy generation rate ($W/m^3 \cdot K$)
$T_{cf,i}$	cold fluid inlet temperature (K)
$T_{cf,o}$	cold fluid outlet temperature (K)
$T_{hf,i}$	hot fluid inlet temperature (K)
$T_{hf,o}$	hot fluid output temperature (K)
\bar{T}	average temperature (K)
T'	temperature fluctuation (K)
U	average velocity (m/s)
V_{bf}	volume of base fluid (L)
V_{np}	volume of nanoparticles = $\frac{m_{np}}{\rho_{np}}$ (L)
\bar{v}	average velocity (m/s)
v'	fluctuating velocity (m/s)
ρ	density (kg/m^3)
ρ_{bf}	density of base fluid (kg/m^3)
ρ_{hnf}	density of hybrid nanofluid (kg/m^3)
ρ_{nf}	density of nanofluid (kg/m^3)
ρ_{np}	density of nanoparticles (kg/m^3)
ρ_{np1}	density of nanoparticle1 (kg/m^3)
ρ_{np2}	density of nanoparticle2 (kg/m^3)
μ	dynamic viscosity ($Pa \cdot s$)
μ_{bf}	viscosity of base fluid ($Pa \cdot s$)
μ_{nf}	viscosity of nanofluid ($Pa \cdot s$)
ϕ_{hnf}	volume fraction of hybrid nanofluid (%)
ϕ_{np1}	volume fraction of nanoparticle1 (%)
ϕ_{np2}	volume fraction of nanoparticle2 (%)
λ	thermal conductivity ($W/m \cdot K$)
λ_{eff}	effective thermal conductivity ($W/m \cdot K$)

λ_t	turbulent thermal conductivity (W/m·K)
∇	gradient operator
ω	specific dissipation rate (s^{-1})

References

- Kim, H.J.; Lee, S.H.; Lee, J.H.; Jang, S.P. Effect of particle shape on suspension stability and thermal conductivities of water-based boehmite alumina nanofluids. *Energy* **2015**, *90*, 1290–1297. [[CrossRef](#)]
- Xie, H.Q.; Wang, J.C.; Xi, T.G.; Liu, Y. Thermal conductivity of suspensions containing nanosized SiC particles. *Int. J. Thermophys.* **2002**, *23*, 571–580. [[CrossRef](#)]
- Murshed, S.M.S.; Leong, K.C.; Yang, C. Enhanced thermal conductivity of TiO₂–Water based nanofluids. *Int. J. Therm. Sci.* **2005**, *44*, 367–373. [[CrossRef](#)]
- Timofeeva, E.V.; Routbort, J.L.; Singh, D. Particle shape effects on thermophysical properties of alumina nanofluids. *J. Appl. Phys.* **2009**, *106*, 014304. [[CrossRef](#)]
- Maheshwary, P.B.; Handa, C.C.; Nemade, K.R. A comprehensive study of effect of concentration, particle size and particle shape on thermal conductivity of titania/water based nanofluid. *Appl. Therm. Eng.* **2017**, *119*, 79–88. [[CrossRef](#)]
- Singh, D.; Timofeeva, E.; Yu, W.; Routbort, J.; France, D.; Smith, D.; Lopez-Cepero, J.M. An investigation of silicon carbide-water nanofluid for heat transfer applications. *J. Appl. Phys.* **2009**, *105*, 064306. [[CrossRef](#)]
- Jeong, J.; Li, C.; Kwon, Y.; Lee, J.; Kim, S.H.; Yun, R. Particle shape effect on the viscosity and thermal conductivity of ZnO nanofluids. *Int. J. Refrig.* **2013**, *36*, 2233–2241. [[CrossRef](#)]
- Zhang, L.; Yu, W.; Zhu, D.; Xie, H.; Huang, G. Enhanced thermal conductivity for nanofluids containing silver nanowires with different shapes. *J. Nanomater.* **2017**, *2017*, 5802016. [[CrossRef](#)]
- Nithiyantham, U.; González-Fernández, L.; Grosu, Y.; Zaki, A.; Igartua, J.M.; Faik, A. Shape effect of Al₂O₃ nanoparticles on the thermophysical properties and viscosity of molten salt nanofluids for TES application at CSP plants. *Appl. Therm. Eng.* **2020**, *169*, 114942. [[CrossRef](#)]
- Vanaki, S.M.; Mohammed, H.A.; Abdollahi, A.; Wahid, M.A. Effect of nanoparticle shapes on the heat transfer enhancement in a wavy channel with different phase shifts. *J. Mol. Liq.* **2014**, *196*, 32–42. [[CrossRef](#)]
- Mahian, O.; Kianifar, A.; Heris, S.Z.; Wongwises, S. First and second laws analysis of a minichannel-based solar collector using boehmite alumina nanofluids: Effects of nanoparticle shape and tube materials. *Int. J. Heat Mass Transf.* **2014**, *78*, 1166–1176. [[CrossRef](#)]
- Akbar, N.S.; Butt, A.W.; Tripathi, D. Nanoparticle shapes effects on unsteady physiological transport of nanofluids through a finite length non-uniform channel. *Results Phys.* **2017**, *7*, 2477–2484. [[CrossRef](#)]
- Bahiraee, M.; Monavari, A.; Naseri, M.; Moayedi, H. Irreversibility characteristics of a modified microchannel heat sink operated with nanofluid considering different shapes of nanoparticles. *Int. J. Heat Mass Transf.* **2020**, *151*, 119359. [[CrossRef](#)]
- Sheikholeslami, M.; Shamlooei, M.; Moradi, R.J.C.E. Numerical simulation for heat transfer intensification of nanofluid in a porous curved enclosure considering shape effect of Fe₃O₄ nanoparticles. *Chem. Eng. Process.* **2018**, *124*, 71–82. [[CrossRef](#)]
- Sheikholeslami, M.; Shehzad, S.A. Numerical analysis of Fe₃O₄–H₂O nanofluid flow in permeable media under the effect of external magnetic source. *Int. J. Heat Mass Transf.* **2018**, *118*, 182–192. [[CrossRef](#)]
- Nguyen, T.K.; Saidizad, A.; Jafaryar, M.; Sheikholeslami, M.; Gerdroodbary, M.B.; Moradi, R.; Li, Z. Influence of various shapes of CuO nanomaterial on nanofluid forced convection within a sinusoidal channel with obstacles. *Chem. Eng. Res. Des.* **2019**, *146*, 478–485. [[CrossRef](#)]
- Hatami, M.; Jafaryar, M.; Zhou, J.; Jing, D. Investigation of engines radiator heat recovery using different shapes of nanoparticles in H₂O/(CH₂OH)₂ based nanofluids. *Int. J. Hydrogen Energy* **2017**, *42*, 10891–10900. [[CrossRef](#)]
- Kim, H.J.; Lee, S.H.; Kim, S.B.; Jang, S.P. The effect of nanoparticle shape on the thermal resistance of a flat-plate heat pipe using acetone-based Al₂O₃ nanofluids. *Int. J. Heat Mass Transf.* **2016**, *92*, 572–577. [[CrossRef](#)]
- Bahiraee, M.; Monavari, A. Thermohydraulic characteristics of a micro plate heat exchanger operated with nanofluid considering different nanoparticle shapes. *Appl. Therm. Eng.* **2020**, *179*, 115621. [[CrossRef](#)]
- Vo, D.D.; Alsarraf, J.; Moradikazerouni, A.; Afrand, M.; Salehipour, H.; Qi, C. Numerical investigation of γ -AlOOH nano-fluid convection performance in a wavy channel considering various shapes of nanoadditives. *Powder Technol.* **2019**, *345*, 649–657. [[CrossRef](#)]
- Khan, U.; Ahmed, N.; Mohyud-Din, S.T. Analysis of magnetohydrodynamic flow and heat transfer of Cu–water nanofluid between parallel plates for different shapes of nanoparticles. *Neural Comput. Appl.* **2018**, *29*, 695–703. [[CrossRef](#)]
- Raza, J.; Mebarek-Oudina, F.; Chamkha, A.J. Magnetohydrodynamic flow of molybdenum disulfide nanofluid in a channel with shape effects. *Multidiscip. Model. Mater. Struct.* **2019**, *15*, 737–757. [[CrossRef](#)]
- Gireesha, B.J.; Sindhu, S. Entropy generation analysis of nanoliquid flow through microchannel considering heat source and different shapes of nanoparticle. *Int. J. Numer. Methods Heat Fluid Flow* **2019**, *30*, 1457–1477. [[CrossRef](#)]
- Elias, M.M.; Miqdad, M.; Mahbulbul, I.M.; Saidur, R.; Kamalisarvestani, M.; Sohel, M.R.; Amalina, M.A. Effect of nanoparticle shape on the heat transfer and thermodynamic performance of a shell and tube heat exchanger. *Int. Commun. Heat Mass Transf.* **2013**, *44*, 93–99. [[CrossRef](#)]

25. Elias, M.M.; Shahrul, I.M.; Mahbulbul, I.M.; Saidur, R.; Rahim, N.A. Effect of different nanoparticle shapes on shell and tube heat exchanger using different baffle angles and operated with nanofluid. *Int. J. Heat Mass Transf.* **2014**, *70*, 289–297. [[CrossRef](#)]
26. Shahsavari, A.; Rahimi, Z.; Salehipour, H. Nanoparticle shape effects on thermal-hydraulic performance of boehmite alumina nanofluid in a horizontal double-pipe minichannel heat exchanger. *Heat Mass Transf.* **2019**, *55*, 1741–1751. [[CrossRef](#)]
27. Alsarraf, J.; Moradikazerouni, A.; Shahsavari, A.; Afrand, M.; Salehipour, H.; Tran, M.D. Hydrothermal analysis of turbulent boehmite alumina nanofluid flow with different nanoparticle shapes in a minichannel heat exchanger using two-phase mixture model. *Phys. A Stat. Mech. Appl.* **2019**, *520*, 275–288. [[CrossRef](#)]
28. Al-Rashed, A.A.; Ranjbarzadeh, R.; Aghakhani, S.; Soltanimehr, M.; Afrand, M.; Nguyen, T.K. Entropy generation of boehmite alumina nanofluid flow through a minichannel heat exchanger considering nanoparticle shape effect. *Phys. A Stat. Mech. Appl.* **2019**, *521*, 724–736. [[CrossRef](#)]
29. Monfared, M.; Shahsavari, A.; Bahrebar, M.R. Second law analysis of turbulent convection flow of boehmite alumina nanofluid inside a double-pipe heat exchanger considering various shapes for nanoparticle. *J. Therm. Anal. Calorim.* **2019**, *135*, 1521–1532. [[CrossRef](#)]
30. Sadripour, S.; Chamkha, A.J. The effect of nanoparticle morphology on heat transfer and entropy generation of supported nanofluids in a heat sink solar collector. *Therm. Sci. Eng. Prog.* **2019**, *9*, 266–280. [[CrossRef](#)]
31. Liu, J.B.; Bayati, M.; Abbas, M.; Rahimi, A.; Naderi, M. Mesoscopic approach for simulating nanofluid flow and heat transfer in a finned multi-pipe heat exchanger. *Int. J. Numer. Methods Heat Fluid Flow* **2019**, *29*, 2822–2839. [[CrossRef](#)]
32. Ghadikolaei, S.S.; Yassari, M.; Sadeghi, H.; Hosseinzadeh, K.; Ganji, D.D. Investigation on thermophysical properties of TiO₂-Cu/H₂O hybrid nanofluid transport dependent on shape factor in MHD stagnation point flow. *Powder Technol.* **2017**, *322*, 428–438. [[CrossRef](#)]
33. Ghadikolaei, S.S.; Hosseinzadeh, K.; Ganji, D.D. Investigation on three dimensional squeezing flow of mixture base fluid (ethylene glycol-water) suspended by hybrid nanoparticle (Fe₃O₄-Ag) dependent on shape factor. *J. Mol. Liq.* **2018**, *262*, 376–388. [[CrossRef](#)]
34. Dinarvand, S.; Rostami, M.N.; Pop, I. A novel hybridity model for TiO₂-CuO/water hybrid nanofluid flow over a static/moving wedge or corner. *Sci. Rep.* **2019**, *9*, 1–11. [[CrossRef](#)]
35. Bhattad, A.; Sarkar, J. Effects of nanoparticle shape and size on the thermohydraulic performance of plate evaporator using hybrid nanofluids. *J. Therm. Anal. Calorim.* **2019**, *143*, 767–779. [[CrossRef](#)]
36. Benkhedda, M.; Boufendi, T.; Tayebi, T.; Chamkha, A.J. Convective heat transfer performance of hybrid nanofluid in a horizontal pipe considering nanoparticles shapes effect. *J. Therm. Anal. Calorim.* **2020**, *140*, 411–425. [[CrossRef](#)]
37. Ghobadi, A.H.; Hassankolaei, M.G. A numerical approach for MHD Al₂O₃-TiO₂/H₂O hybrid nanofluids over a stretching cylinder under the impact of shape factor. *Heat Transf. Asian Res.* **2019**, *48*, 4262–4282. [[CrossRef](#)]
38. Aziz, A.; Jamshed, W.; Ali, Y.; Shams, M. Heat transfer and entropy analysis of Maxwell hybrid nanofluid including effects of inclined magnetic field, Joule heating and thermal radiation. *Discret. Contin. Dyn. Syst. S* **2020**, *13*, 2667. [[CrossRef](#)]
39. Ghadikolaei, S.S.; Hosseinzadeh, K.; Ganji, D.D. Investigation on ethylene glycol-water mixture fluid suspend by hybrid nanoparticles (TiO₂-CuO) over rotating cone with considering nanoparticles shape factor. *J. Mol. Liq.* **2018**, *272*, 226–236. [[CrossRef](#)]
40. Ghadikolaei, S.S.; Gholinia, M.; Hoseini, M.E.; Ganji, D.D. Natural convection MHD flow due to MoS₂-Ag nanoparticles suspended in C₂H₆O₂H₂O hybrid base fluid with thermal radiation. *J. Taiwan Inst. Chem. Eng.* **2019**, *97*, 12–23. [[CrossRef](#)]
41. Ghadikolaei, S.S.; Gholinia, M. 3D mixed convection MHD flow of GO-MoS₂ hybrid nanoparticles in H₂O-(CH₂OH)₂ hybrid base fluid under the effect of H₂ bond. *Int. Commun. Heat Mass Transf.* **2020**, *110*, 104371. [[CrossRef](#)]
42. Maraj, E.N.; Iqbal, Z.; Azhar, E.; Mehmood, Z. A comprehensive shape factor analysis using transportation of MoS₂-SiO₂/H₂O inside an isothermal semi vertical inverted cone with porous boundary. *Results Phys.* **2018**, *8*, 633–641. [[CrossRef](#)]
43. Sahu, M.; Sarkar, J. Steady-state energetic and exergetic performances of single-phase natural circulation loop with hybrid nanofluids. *J. Heat Transf.* **2019**, *141*, 082401. [[CrossRef](#)]
44. Garud, K.S.; Seo, J.H.; Patil, M.S.; Bang, Y.M.; Pyo, Y.D.; Cho, C.P.; Lee, M.Y. Thermal–electrical–structural performances of hot heat exchanger with different internal fins of thermoelectric generator for low power generation application. *J. Therm. Anal. Calorim.* **2021**, *143*, 387–419. [[CrossRef](#)]
45. Garud, K.S.; Seo, J.H.; Cho, C.P.; Lee, M.Y. Artificial neural network and adaptive neuro-fuzzy interface system modelling to predict thermal performances of thermoelectric generator for waste heat recovery. *Symmetry* **2020**, *12*, 259. [[CrossRef](#)]
46. Dadsetani, R.; Sheikhzadeh, G.A.; Safaei, M.R.; Leon, A.S.; Goodarzi, M. Cooling enhancement and stress reduction optimization of disk-shaped electronic components using nanofluids. *Symmetry* **2020**, *12*, 931. [[CrossRef](#)]
47. Seo, J.H.; Garud, K.S.; Lee, M.Y. Grey relational based Taguchi analysis on thermal and electrical performances of thermoelectric generator system with inclined fins hot heat exchanger. *Appl. Therm. Eng.* **2021**, *184*, 116279. [[CrossRef](#)]
48. Bahiraeei, M.; Monavari, A.; Moayedeei, H. Second law assessment of nanofluid flow in a channel fitted with conical ribs for utilization in solar thermal applications: Effect of nanoparticle shape. *Int. J. Heat Mass Transf.* **2020**, *151*, 119387. [[CrossRef](#)]
49. Lee, M.Y.; Seo, J.H.; Lee, H.S.; Garud, K.S. Power generation, efficiency and thermal stress of thermoelectric module with leg geometry, material, segmentation and two-stage arrangement. *Symmetry* **2020**, *12*, 786. [[CrossRef](#)]
50. Ooi, E.H.; Popov, V. Numerical study of influence of nanoparticle shape on the natural convection in Cu-water nanofluid. *Int. J. Therm. Sci.* **2013**, *65*, 178–188. [[CrossRef](#)]

51. Garud, K.S.; Lee, M.Y. Numerical Investigations on Heat Transfer Characteristics of Single Particle and Hybrid Nanofluids in Uniformly Heated Tube. *Symmetry* **2021**, *13*, 876. [[CrossRef](#)]
52. Sanches, M.; Marseglia, G.; Ribeiro, A.P.; Moreira, A.L.; Moita, A.S. Nanofluids Characterization for Spray Cooling Applications. *Symmetry* **2021**, *13*, 788. [[CrossRef](#)]
53. Arani, A.A.A.; Sadripour, S.; Kermani, S. Nanoparticle shape effects on thermal-hydraulic performance of boehmite alumina nanofluids in a sinusoidal-wavy mini-channel with phase shift and variable wavelength. *Int. J. Mech. Sci.* **2017**, *128*, 550–563. [[CrossRef](#)]
54. Ghachem, K.; Aich, W.; Kolsi, L. Computational analysis of hybrid nanofluid enhanced heat transfer in cross flow micro heat exchanger with rectangular wavy channels. *Case Stud. Therm. Eng.* **2021**, *24*, 100822. [[CrossRef](#)]
55. Bhattad, A.; Sarkar, J.; Ghosh, P. Energy-economic analysis of plate evaporator using brine-based hybrid nanofluids as secondary refrigerant. *Int. J. Air-Cond. Refrig.* **2018**, *26*, 1850003. [[CrossRef](#)]
56. Arun, K.R.; Kunal, G.; Srinivas, M.; Kumar, C.S.; Mohanraj, M.; Jayaraj, S. Drying of untreated Musa nendra and Momordica charantia in a forced convection solar cabinet dryer with thermal storage. *Energy* **2020**, *192*, 116697. [[CrossRef](#)]
57. Kwon, J.T.; Nahm, T.H.; Kim, T.W.; Kwon, Y.C. An Experimental study on pressure drop and heat transfer coefficient of laminar Ag nanofluid flow in mini-tubes. *J. Korea Acad. Ind. Coop. Soc.* **2009**, *10*, 3525–3532.
58. Zheng, D.; Wang, J.; Chen, Z.; Baleta, J.; Sundén, B. Performance analysis of a plate heat exchanger using various nanofluids. *Int. J. Heat Mass Transf.* **2020**, *158*, 119993. [[CrossRef](#)]
59. Tiwari, A.K.; Ghosh, P.; Sarkar, J. Heat transfer and pressure drop characteristics of CeO₂/water nanofluid in plate heat exchanger. *Appl. Therm. Eng.* **2013**, *57*, 24–32. [[CrossRef](#)]
60. Kim, N.H. An experimental investigation on the air-side performance of fin-and-tube heat exchangers having radial slit fins. *Int. J. Air-Cond. Refrig.* **2015**, *23*, 1550021. [[CrossRef](#)]
61. Tiwari, A.K.; Ghosh, P.; Sarkar, J. Performance comparison of the plate heat exchanger using different nanofluids. *Exp. Therm. Fluid Sci.* **2013**, *49*, 141–151. [[CrossRef](#)]
62. Singh, S.K.; Sarkar, J. Improving hydrothermal performance of hybrid nanofluid in double tube heat exchanger using tapered wire coil turbulator. *Adv. Powder Technol.* **2020**, *31*, 2092–2100. [[CrossRef](#)]
63. Raj, A.K.; Kunal, G.; Srinivas, M.; Jayaraj, S. Performance analysis of a double-pass solar air heater system with asymmetric channel flow passages. *J. Therm. Anal. Calorim.* **2019**, *136*, 21–38. [[CrossRef](#)]
64. Alm, B.; Imke, U.; Knitter, R.; Schygulla, U.; Zimmermann, S. Testing and simulation of ceramic micro heat exchangers. *Chem. Eng. J.* **2008**, *135*, S179–S184. [[CrossRef](#)]
65. Ghosh, M.M.; Ghosh, S.; Pabi, S.K. Effects of particle shape and fluid temperature on heat-transfer characteristics of nanofluids. *J. Mater. Eng. Perform.* **2013**, *22*, 1525–1529. [[CrossRef](#)]
66. Garud, K.S.; Seo, J.H.; Lee, M.Y. Effect of Guide Fin Structures and Boundary Parameters on Thermal Performances of Heat Exchanger for Waste Heat Recovery Thermoelectric Generator. *J. Korea Acad. Ind. Coop. Soc.* **2021**, *22*, 30–35.